MECHANISMS FOR METHANE TRANSPORT AND HYDRATE ACCUMULATION IN COARSE-GRAINED RESERVOIRS

Final Scientific/Technical Report

September 1, 2013 – March 31, 2018

Hugh Daigle, University of Texas at Austin
Steven Bryant, University of Texas at Austin/University of Calgary
Kishore Mohanty, University of Texas at Austin
Ann Cook, Ohio State University
Alberto Malinverno, Lamont-Doherty Earth Observatory

Date Issued: June 2018

DOE Award Number DE-FE0013919

Submitting Organization
University of Texas at Austin
101 E 27th St.
Suite 5.300
Austin, TX 78712

Subaward Recipients
Ohio State University
125 S Oval Mall
Columbus, OH 43210-1308

Lamont-Doherty Earth Observatory
Columbia University
61 Route 9W
Palisades, NY 10964-8000

Disclaimer

This report was prepared as an account of work sponsored by an agency of the United States Government. Neither the United States Government nor any agency thereof, nor any of their employees, makes any warranty, express or implied, or assumes any legal liability or responsibility for the accuracy, completeness, or usefulness of any information, apparatus, product, or process disclosed, or represents that its use would not infringe privately owned rights. Reference herein to any specific commercial product, process, or service by trade name, trademark, manufacturer, or otherwise does not necessarily constitute or imply its endorsement, recommendation, or favoring by the United States Government or any agency thereof. The views and opinions of authors expressed herein do not necessarily state or reflect those of the United States Government or any agency thereof.

Abstract

The distribution of natural methane hydrate within high saturation reservoirs and mechanisms that control the migration of methane are an active area of research. In this project, we studied methane migration mechanisms and associated hydrate accumulation rates in coarse-grained sands of the Terrebonne Basin, located in Walker Ridge Block 313 (WR313), northern Gulf of Mexico. Hydrate in this area is distributed heterogeneously within ~900 m of methane hydrate stability zone, in both thick (10-25 m) and thin (< 3 m) sand layers, and in units of subvertical hydrate-filled fractures. We investigated hydrate formation from diffusively and advectively supplied methane using one-, two-, and three-dimensional basin modeling with inputs from well log and seismic data. The hydrate accumulations at WR313 can mostly be explained by short, diffusive migration of methane as well as short-range advective transport of methane from clays into neighboring coarser-grained layers. This is likely enhanced by small-scale lithologic variations, including local microbial methanogenesis in interbedded clays. Furthermore, our work shows overpressure in clay sediments surrounding sand reservoirs may enhance short-range diffusive migration. Long-range migration of dissolved methane and gas mainly influence hydrate saturation right at the base of the hydrate stability zone, although the dissolved phase can be channeled upwards along sands by compaction-driven flow. Capillary effects can allow gas bubbles to migrate appreciable distances above the predicted base of gas hydrate stability, possibly reaching a few tens of meters into the hydrate stability zone. Recycling methane from hydrate buried beneath the base of the hydrate stability zone can concentrate hydrate at large saturations within a few tens of meters of the base of hydrate stability.

Table of Contents

Executive summary iv

1. Introduction 1
    1.1 Background 1
    1.2 Hydrate distribution in the Terrebonne Basin 2

2. Modeling methods 6
    2.1 Conservation of mass and energy 7
    2.2 Capillary controls on hydrate and free gas growth in pores 14
        2.2.1 Two-phase (hydrate-aqueous and gas aqueous) systems 14
        2.2.2 Three-phase (hydrate-gas-aqueous) systems 16
    2.3 Parameterizing the subsurface 22
        2.3.1 Parameterizing pore size distributions 22
        2.3.2 Microbial methanogenesis 25
        2.3.3 Simulation reference frames 26
        2.3.4 Incorporating heterogeneity from seismic data 28

3. Hydrate formation from dissolved methane 30
    3.1 Short migration 30
    3.2 Advective transport 33
    3.3 Remarks on dissolved methane 35

4. The role of a discrete gas phase 39
    4.1 Introduction 39
    4.2 Modeling methane recycling 40
    4.3 Methane flux necessary to form a gas phase 45

5. Conclusions 45

References 46

List of acronyms and abbreviations 51

Executive summary

Thick accumulations of methane hydrate at high saturations in the pore space – termed massive methane hydrate deposits – have attracted significant attention recently as targets for resource exploitation. Understanding how these types of methane hydrate deposits form remains a key question. In this project, we focused on methane migration mechanisms and associated methane hydrate accumulation rates in coarse-grained sands of the Terrebonne Basin, located in Walker Ridge Block 313 in the northern Gulf of Mexico (WR313). Using a combination of one-, two-, and three-dimensional basin modeling, we focused on two different methane migration mechanisms to form high-saturation hydrate-bearing sand layers: diffusive flux and advective transport of dissolved methane. In the case of diffusive flux, methane is generated microbially in finer-grained sediments and diffuses over short distances into adjacent sand layers where capillary effects favor precipitation of hydrate, which is called short migration. In the case of advective transport, methane may be supplied either by long-distance flow along permeable layers into the MHSZ, called long migration, or by short-distance advection of microbial methane that is focused into more permeable layers by compaction-driven flow, called short advection.

These different migration mechanisms have distinct timescales and hydrate accumulation patterns. For example, diffusion into coarse-grained layers tends to form heterogeneous hydrate deposits, with hydrate concentrated on the upper and lower edges of the coarse-grained layers with little to no hydrate in the middle of the layers. Maximum hydrate saturations in these cases can be 30-40% of the pore space after ~1 Myr based on our simulations of the hydrate system at WR313. At the basin scale, individual sand layers compete for methane produced in intervening clay layers. Because microbial methane is mostly generated at shallow depths, hydrate may only be preserved from dissolution in sands during burial through the MHSZ if fracture- or vein-hosted hydrates form in adjacent clays, providing an additional supply of methane during burial. These fracture-hosted hydrates may form in response to transient deposition of organic-rich sediment at the seafloor, particularly on glacial-interglacial timescales, resulting in episodes of intense microbial methanogenesis.

If sedimentation rates are rapid enough to generate significant overpressure, compaction-driven flow can serve as an additional mechanism of focusing microbial methane into coarse-grained layers that act as conduits for fluid flow. Our work suggests that these conditions are met at WR313. Under these conditions, hydrate may fill 30-40% of the pore space after ~1 Myr, with hydrate distributed more homogeneously within sand layers, including far updip within the MHSZ. These saturations may be further enhanced by interbedding of sands and thin clay layers in which further microbial methanogenesis occurs, providing a local source of methane that may be flushed into adjacent coarser-grained layers and form hydrate.

Finally, we found that recycling of methane as the BHSZ can provide a significant source of methane to form hydrate above the BHSZ, and that pore size effects allow gas to coexist with hydrate for tens of m above the BHSZ, even in sandy sediments. This may be a mechanism of delivering recycled methane to much shallower depths within the MHSZ, and could reduce the amount of microbial methane that is necessary to form massive hydrate deposits.

Comparisons to other sites worldwide suggests that WR313 has much higher microbial methanogenesis rates than other locations, and lower advective methane migration rates. The result of these differences on the development of massive hydrate deposits seems to be minimal, since more rapid microbial methanogenesis can make up for a comparative lack of methane supply by long migration. Our work has demonstrated the importance of microbial methanogenesis, short-distance migration, pore water advection, and lithologic heterogeneity on generating the massive hydrate deposits in the Terrebonne Basin.

1. Introduction

1.1 Background

Massive methane hydrate deposits, defined as thick accumulations of high hydrate saturation, have been encountered in many regions worldwide, including the Nankai Trough offshore Japan (Tsuji et al., 2008; Tamaki et al., 2017), the Krishna-Godavari Basin offshore India (Collett et al., 2008; Kumar et al., 2016), the Ulleung Basin offshore Korea (Kang et al., 2006; Kim et al., 2011), and the outer continental shelf of the Gulf of Mexico (Boswell et al., 2012; Flemings et al., 2017). As hydrates begin to be exploited as an energy resource, it is becoming more important to understand the mechanisms that lead to development of massive hydrate deposits in coarse-grained sediments, which are the most attractive reservoirs for exploration and production activities (e.g., Moridis et al., 2008). Massive hydrate deposits require a methane source, migration mechanisms, a reservoir, and an appropriate seal. Hydrate reservoirs and seals are defined by thermodynamics rather than by buoyancy, as in the case of conventional oil and gas. Hydrates form most easily within coarse-grained sediments within the methane hydrate stability zone (MHSZ), the depth interval in which pressure and temperature favor hydrate as the stable phase. Methane sources may be microbial as well as thermogenic (Rice and Claypool, 1981). In this project, we focused on methane migration mechanisms as they represent some of the least understood processes in hydrate systems, but at the same time represent a crucial link between sites of methane generation and hydrate reservoirs.

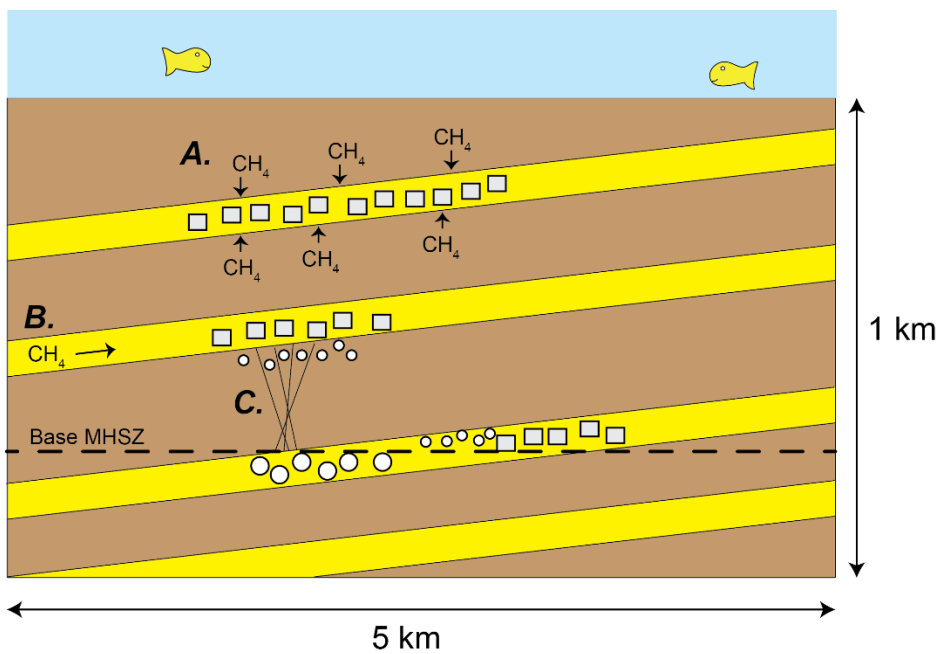

Figure 1. Illustration of methane (circles) migration mechanisms associated with development and persistence of massive hydrate deposits (squares). Yellow layers represent coarser-grained units; brown represents finer-grained, clay-rich units. A: Short migration of methane from fine-grained layers into adjacent coarser-grained layers to form hydrate. B: Long migration of dissolved methane into the MHSZ. C: Methane migration in free gas phase within the MHSZ, either locally produced in fine-grained units or through fractures connected to the base of the MHSZ where gas may accumulate as hydrate-bearing units are buried, or updip from the base of the MHSZ within a coarse-grained unit.

Migration of methane into the MHSZ may occur in the dissolved phase or as a free gas phase. The methane flux and the phase of supplied methane determine the rate of hydrate formation, the amount of hydrate formed, and its distribution (Daigle and Dugan, 2010a). The evolution and persistence of massive hydrate deposits therefore require a sufficient methane supply. We envision three migration mechanisms as illustrated in Figure 1: (A) diffusive flux within the MHSZ of dissolved methane from finer-grained units into coarser-grained units where hydrate forms preferentially, known as short migration; (B) advective flux of dissolved methane from a source at depth into the MHSZ, known as long migration; or (C) migration of methane in the free gas phase, either produced locally within the MHSZ or supplied from the base of the MHSZ from long migration or from recycling of hydrate that is buried beneath the base of the MHSZ.

The relative time scales and fluxes associated with these three migration mechanisms are largely unconstrained, but chiefly control the development and longevity of massive hydrate deposits that are attractive to energy resource development. To evaluate different migration mechanisms, we developed 1-D, 2-D, and 3-D reservoir models (Davie and Buffett, 2001; Sun and Mohanty, 2006) and used seismic data from WesternGeco and well log data collected during the Chevron-led Gulf of Mexico Gas Hydrate Joint Industry Project (JIP) Leg 2 (Boswell et al., 2010) at Walker Ridge Block 313 (WR313) in the Terrebonne Basin as a case study to answer the following questions:

1. What are the dissolved methane flux, organic matter abundance, and time required to develop massive hydrate accumulations by short-distance migration of microbial methane generated within fine-grained sediments into adjacent coarse-grained layers?
2. What are the dissolved methane flux and time required to develop massive hydrate accumulations by long-distance, updip migration?
3. Is dissolved methane sufficient to produce massive hydrate deposits, or is a gas phase required to exist within the MHSZ? If so, what are the conditions for three-phase equilibrium?
4. What is the fate of hydrate that subsides beneath the base of the MHSZ? How much free gas accumulates below the base of the MHSZ, and what is the overpressure associated with gas accumulation? Does this gas contribute to massive hydrate accumulations, returning to the MHSZ by vertical migration through fractures or by along-dip migration through permeable strata, or does this gas make no contribution at all because it is this gas simply trapped and buried beneath the MHSZ?

1.2 Hydrate distribution in the Terrebonne Basin

Natural gas hydrates were first suspected in the northwestern Walker Ridge area by McConnell and Kendall (2002), who observed dim-outs (or phase-reversals) on 3-D seismic data that were thought to signal the transition from free gas to gas hydrate in permeable sand units. In 2009, JIP Leg 2 drilled two logging-while drilling (LWD) holes, Hole G and Hole H in WR313, on the edge of a salt withdrawal minibasin in 1950 m of water (Hutchinson et al., 2008; Boswell et al.,

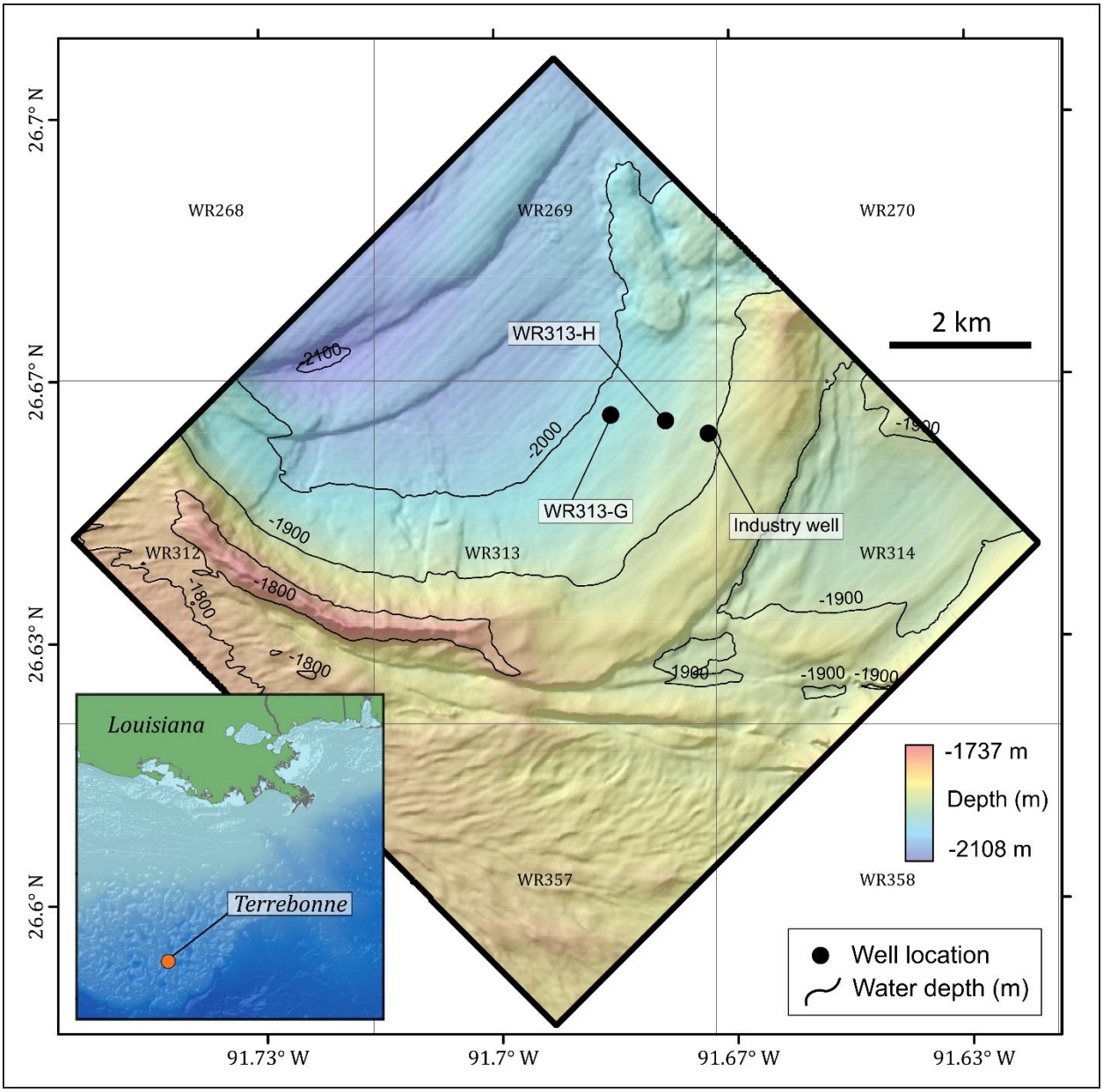

Figure 2. Location of the Terrebonne Basin in the Gulf of Mexico. Bathymetry from Kramer and Shedd (2017).

2010) (Fig. 2). The base of the MHSZ at the WR313 site is about 900 mbsf (meters below seafloor). These holes were located updip of some high-amplitude phase reversals visible on seismic data (Fig. 3). The high gas hydrate saturations confirmed the high-amplitude phase reversals on the seismic data were caused by a free gas-to-gas hydrate transition (McConnell et al., 2010). Many more phase reversal regions have now been identified on seismic data in the Gulf of Mexico and are referred to as 'partial BSRs' (bottom simulating reflections; Shedd et al., 2012; Hillman et al., 2017), suggesting many areas similar to WR313 site may exist.

As part of our work, we mapped seismic data and reanalyzed well logs (Fig. 4) in the orange, blue and green target sand layers in Nole et al., (2017). Logging-while-drilling measurements revealed that the Blue sand unit contains sandy layers interbedded with clays for a total hydrate-

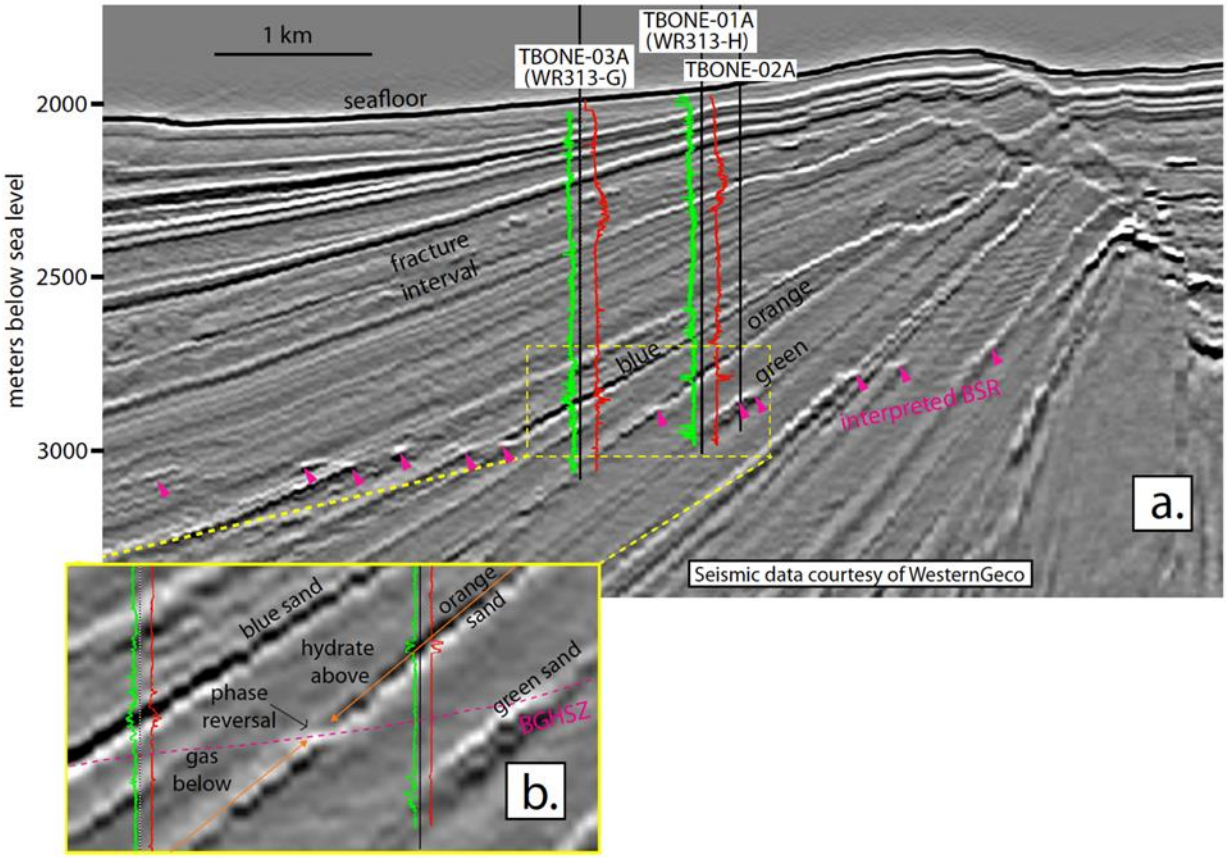

Figure 3. A seismic cross section at WR313 through the two JIP Leg 2 holes, Hole G and Hole H as well as planned wells for GOM2-02. The gamma ray log (GR), a lithology indicator, is shown in green at each hole. A propagation resistivity log (RES) is shown in red. The main sands modeled in this study are identified: the red sand, the blue sand and the orange sand units. A clear phase reversal can be seen near Hole H, slightly down-dip from the orange sand unit. A strata-bound, clay-rich interval containing fracture-hosted hydrate occurs within the MHSZ.

filled sand of 25 m, whereas the deeper. Orange sand was comprised of two main lobes for a total of 10.5 m of hydrate-filled sand (Fig. 4). Thicknesses reported here are larger than by Frye et al. (2012) and Boswell et al. (2012), as they only considered high saturation ($S_h > 0.5$) gas hydrate. In our models, we are interested not just in high saturations of hydrate, but also in accumulations with lower saturation.

Another 9 m thick sand, the Green sand, lies below the Orange sand. The Green sand was water saturated in Hole WR313-H because it occurred below the MHSZ, but brightening of the green horizon at the BSR in seismic data suggests that it contains hydrate within MHSZ (Frye et al., 2012). A number of thin sand layers (< 3 m) were also identified throughout Holes WR313-G and WR313-H; some sand layers contain gas hydrate and other sand layers are water-saturated. One particular 2.5 m sand, called Unit A by Boswell et al. (2012) and Cook and Malinverno (2013), appears near 290 meters below seafloor (mbsf) within a 150 m thick clay-rich unit containing gas hydrate filled fractures. To maintain consistency with the sand naming scheme in the Terrebonne Basin (i.e. Hillman et al., 2017), we refer to this 2.5 m sand as the Red sand. The Red sand has a combination of interesting characteristics: for example, the hydrate in the sand is

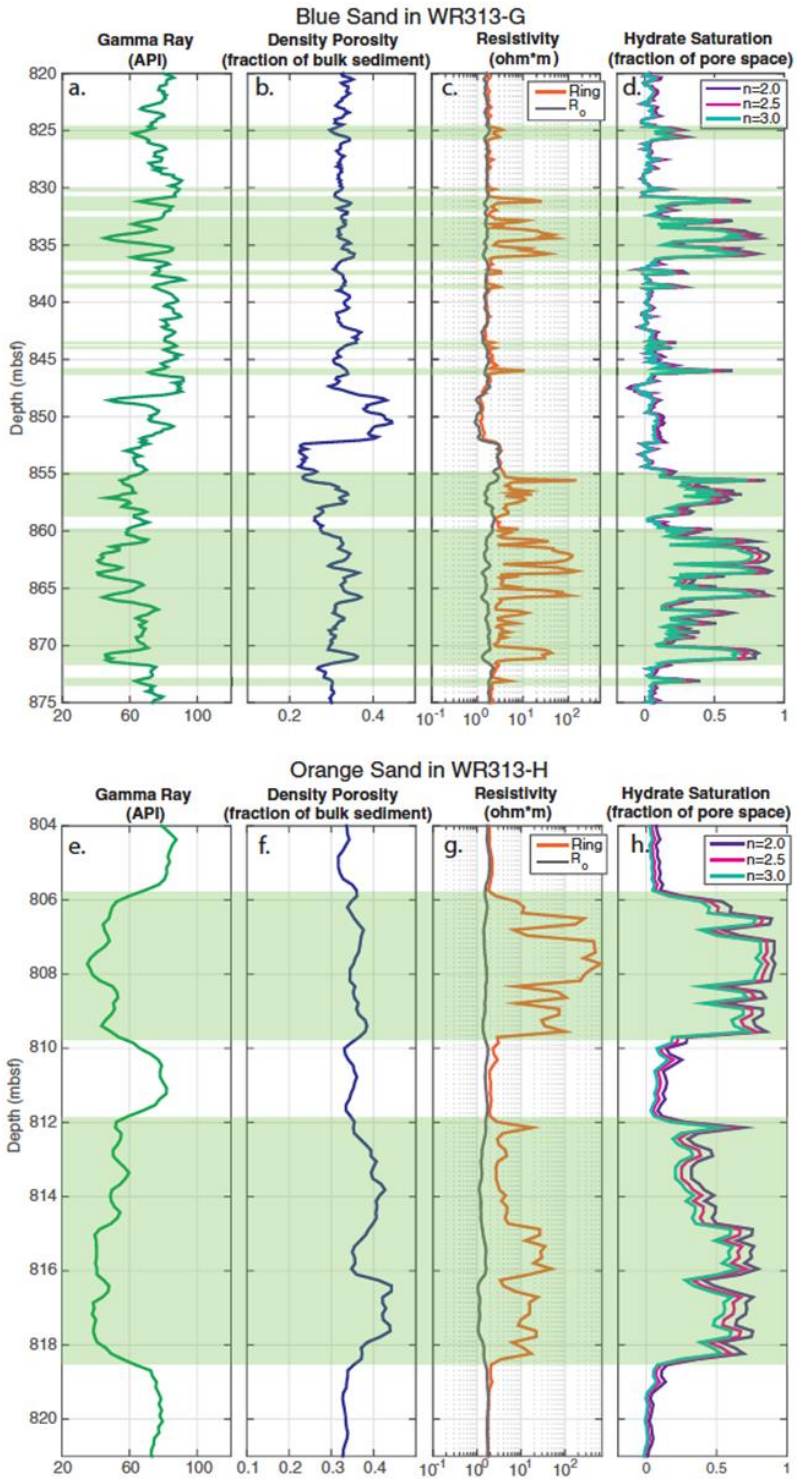

Figure 4. Measured and calculated logs from (a–d) Hole WR313-G Blue sand unit and (e–h) Hole WR313-H Orange sand unit in mbsf. Interpreted hydrate-bearing sands are highlighted in green. Figures 4a and 4e show the measured gamma ray log, which indicates sandier layers to the left (lower API) and clay-rich layers to the right (higher API). Figures 4b and 4f show the density porosity, which is corrected for the hydrate saturation. The measured ring resistivity is shown in Figures 4c and 4g along with calculated Ro, the resistivity of the formation in the absence of hydrate. The calculated hydrate saturation is presented in Figures 4d and 4h. Figure from Nole et al., 2017.

concentrated near the top and bottom of the sand. Surrounding the sand, a hydrate-free zone persists within the bounding clays for several meters before hydrate is again observed in fractures. These features led Cook and Malinverno (2013) to propose that the Red sand could be filled with hydrate as the result of diffusive methane migration from the surrounding clay, which they termed short migration.

While the seismic identification technique and drilling program at Walker Ridge was clearly successful, it remains unclear how the sand layers at Walker Ridge became saturated with natural gas hydrate. The large hydrate saturations are vertically heterogeneous but present through nearly 1 km of sediment within the MHSZ. On the other hand, the large saturations exhibit relatively limited lateral extent, with continuity of perhaps 1 km in a dipping coarse-grained layer (elevated resistivities in any given layer typically occur in one or two but rarely all three wells in Fig. 3). Because of the bright spots observed directly down dip of the base of the MHSZ the gas hydrate saturated sand layers, Boswell et al. (2012) and Frye et al. (2012) conclude that the most likely explanation is lateral migration of natural gas along the sand unit from a deeper source, or "long migration." In contrast, Cook and Malinverno (2013) argue that hydrate in the red sand could have been supplied by short migration. In addition, Cook and Malinverno (2013) note that the presence of free gas below a gas hydrate saturated unit does not necessarily imply that the methane was derived from below, as the free gas below the MHSZ may be the result of dissociated gas hydrate that could have been formed from microbial methane within the MHSZ and eventually buried below the base of the MHSZ.

2. Modeling methods

The simulator we developed is based on the original simulation design outlined in Sun (2005) and Sun and Mohanty (2006). That simulator, developed in FORTRAN, was redeveloped in Matlab and vectorized to improve efficiency. Here we review the general design of the simulator and introduce the important physical models that were added as part of this work to distinguish this software from other methane hydrate reservoir simulators.

This simulator solves a system of coupled partial differential equations describing the transport of methane mass, water mass, and system energy using a 3-D fully implicit finite volume difference scheme. Gas hydrate formation, dissolution, and dissociation are tracked over geologic time in the following simulations. Gas hydrates dissolve within their stability zone when the pore water methane concentration falls below solubility; hydrates dissociate when the local temperature and/or pressure fall outside thermodynamic stability. The characteristic time scale of kinetic inhibition to growth or dissolution of hydrate is assumed to be negligible in comparison to the simulation timescale. Thus, all methane in excess of effective solubility in the aqueous phase is considered to move instantaneously into the free gas and/or hydrate phase; i.e., dissolved methane is always assumed to be in local equilibrium with hydrate or free gas phases. The assumption that hydrate reaction kinetics are fast in comparison to heat and mass transfer has been shown to be valid when describing hydrate accumulation in marine sediments (Rempel and Buffet, 1997; Sun, 2005). The simulator considers four phases (aqueous, ice, hydrate, and free gas), which can contain two components (methane or water). In addition to consuming

methane, hydrate formation excludes any salts that are dissolved in pore water, which locally elevates salinity. The opposite is true during hydrate dissolution and dissociation.

The following assumptions are made in the development of the methane hydrate simulator used in this work:

- Thermodynamic equilibrium prevails over reaction kinetics on geologic timespans.
- Dissolved methane does not affect fluid density.
- The hydrate phase is immobile and moves with sediment.
- Microbial methanogenesis occurs at steady state.
- Labile organic matter available for microbial methanogenesis is a direct function of clay fraction.
- Differences in compaction trends between different lithologies are negligible; the entire system is assumed to compact in the same manner (although porosity, permeability, and pore size can vary across lithology).
- Aqueous methane solubility at hydrate-water equilibrium is a strong function of temperature and a weak function of pressure. So at a given temperature, methane solubility within the MHSZ is determined through Henry's Law by the gas partial pressure at 3-phase equilibrium.
- The mole fraction of methane in the free gas phase is significantly larger than the water vapor mole fraction, so methane partial pressure is equal to the gas pressure.
- Hydrate and free gas are both nonwetting phases.
- Effective pore size occupied by a given phase is a proxy for effective curvature of that phase.
- In determining capillary pressure and how the phase boundary shifts due to capillary effects, pores are considered spherical.
- All hysteresis is neglected.
- Relative permeability in 3-phase systems uses a Brooks-Corey model, which does not consider the potential effect of hydrate crusts at gas-water interfaces on the migration behavior of gas and water.
- Hydrate and free gas co-occupy the large pore space equally at 3-phase equilibrium.

2.1 Conservation of mass and energy

The governing equations are formulated as follows:

$$\frac{\partial}{\partial t}(\varphi C^m) = -\nabla \cdot F^m + Q^m, \tag{1a}$$

$$\frac{\partial}{\partial t}(\varphi C^w) = -\nabla \cdot F^w + Q^w, \tag{1b}$$

$$\frac{\partial U}{\partial t} = -\nabla \cdot F^e + Q^e, \tag{1c}$$

where φ is the sediment porosity, C^m and C^w are the mass concentrations of methane and water per unit pore volume, U is the internal energy of the system per unit volume, F^i describes the sum of the mass fluxes (advective and diffusive) and energy flux (superscript e) of each

component into and out of a control volume, and Q describes sources or sinks of each component in the control volume.

The total masses of each component are calculated by summing the masses of each component in each phase:

$$C^m = x_A^m \rho_A S_A + x_G^m \rho_G S_G + x_H^m \rho_H S_H, \quad (2a)$$

$$C^w = x_A^w \rho_A S_A + x_G^w \rho_G S_G + x_H^w \rho_H S_H + \rho_I S_I, \quad (2b)$$

where x_j^i describes the mass fraction (kg component/kg total) of component i (methane or water) in phase j (water, gas, hydrate, or ice), ρ_j is the density of phase j, and S_j is the saturation of phase j. Ice phase density, ρ_I, is set at 917 kg/m^3. For methane hydrate, ρ_H is assumed to be a constant 924 kg/m^3, and using a hydration number of 6, x_H^m is 0.1252, and x_H^w = 1 - x_H^m = 0.8748 (Sloan and Koh, 2007). For water, ρ_A is the combined density of the water and salt phases and is adjusted for changing salt concentrations; methane mass is considered negligible in this calculation because of its low solubility in water.

Dissolved salt transport is implemented in this simulator primarily as added functionality; in diffusion-dominated and short-advection simulations, salinity gradients are found to have negligible impact on hydrate distribution because of the long timescale over which hydrate accumulation take place (hundreds of thousands of years). Although the diffusion coefficient of methane in pore water is similar to that of salt in pore water, migration of dissolved methane is always occurring because of persistent concentration gradients between fine-grained and coarse-grained material. Changes in salt concentration occur only as a result of hydrate formation, which excludes the salt phase. Methane hydrate stability is only affected when salt concentrations build up. In diffusion-dominated simulations, since enhanced salinity diffuses away as soon as it is generated, and since salinity enhancement is limited by the rate of methane diffusion, salt essentially diffuses away as soon as salinity is enhanced. In short advection simulations, salinity enhancements are washed out with aqueous fluid flow, but the rate at which salinity accumulates depends on the rate at which hydrate is forming, so future work could explore how salt advection affects methane hydrate stability as a function of fluid velocity. Conversion of a free gas phase to hydrate, however, could significantly enhance salinity for significant periods of time (Liu and Flemings, 2006). Methane recycling simulations in this work neglected dissolved salt transport to focus specifically on the dynamics of three-phase (water, gas, and hydrate) systems at local thermodynamic equilibrium.

Pore water salinity is considered assuming that it only exists in the dissolved phase, contributes only to the density of the aqueous phase, controls the phase boundary between methane hydrate and free gas, and doesn't contribute to heat transfer in the system. Therefore, transport of dissolved salt (NaCl) is solved separately and sequentially after solution of the water/methane mass and energy transport equations. Dissolved salt mass transport is solved fully implicitly, and precipitation of a solid salt phase is not considered. In marine hydrate-bearing environments, the phase boundary is affected by the presence of dissolved salt in pore fluid, which inhibits hydrate formation (Koh et al., 2002).

For the purposes of marine sediment simulations, the phase boundary in P-T space can be shifted by a temperature increment ΔT^{hyd} if salt is present in the pore water, given by the following equation (Sloan and Koh, 2007):

$$\frac{\Delta T^{hyd}}{T_W(T_w-\Delta T^{hyd})} = 0.6652\frac{\Delta T^{fus}}{T_f(T_f-\Delta T^{fus})}, \tag{3a}$$

where T_w is the freezing temperature of hydrate in a salt-free system, ΔT^{fus} is the hydrate freezing temperature depression at atmospheric pressure for a given salt mass fraction, and T_f is the freezing temperature of water. The hydrate freezing temperature depression at atmospheric conditions is calculated from data tabulation as follows (Lide, 2004):

$$\Delta T^{fus} = x_A^s(164.49x_A^s + 49.462), \tag{3b}$$

where x_A^s is the mass fraction of salt in the aqueous phase, in kg salt/kg brine. The P-T diagram is thus shifted as follows:

$$T = T_0 + \Delta T^{hyd}, \tag{4}$$

where T_0 is the in situ pore water temperature, and T is the temperature in pure water whose equilibrium pressure would correspond to the equilibrium pressure of a saline system at T_0. In the presence of dissolved salt, hydrate precipitates at a lower temperature for a given pressure (or at a higher P for a given T) compared to pure water.

Mole fractions also add to unity. The mole fraction of water in the vapor phase, n_G^w, is calculated using the partial pressure rule:

$$n_G^w = \frac{P_v}{P_G}, \tag{5}$$

where P_v is the water vapor pressure, determined empirically as a function of temperature (Chapoy et al., 2004; Kim et al., 2003), and P_G is the gas pressure.

In the aqueous phase, the mole fraction of methane is determined according to Henry's Law (Carroll and Mather, 1997; Klauda and Sandler, 2001):

$$n_A^m = \begin{cases} \frac{P_G}{H_m}, P_G < P_e \\ \frac{P_e}{H_m}, P_G \geq P_e \end{cases}, \tag{6}$$

where P_e is the 3-phase equilibrium gas pressure and H_m is the Henry's Law constant for dissolved methane in water and is a function of temperature (Carroll and Mather, 1997). Mass fractions of component i in phase j are then calculated as follows:

$$x_j^i = \frac{n_j^i N^i}{\sum_i n_j^i N^i}, \tag{7}$$

where N^i is the molecular weight of component i.

Phase saturations and mass fractions of components in each phase are subject to the following constraints:

$$\sum_{i=m,w,s} x_j^i = 1 \; \forall \; j \in \{A, G, H\}, \tag{8a}$$

$$\sum_j S_j = 1, \tag{8b}$$

where S_j is the saturation of phase j.

Internal energy of the system is calculated as the weighted average of the internal energy of the solid rock matrix, fluid, and hydrate phases in the pore space as follows:

$$U = \varphi\left(\sum_j \widehat{U}_j S_j \rho_j\right) + (1-\varphi)\rho_R \widehat{U}_R, \tag{9}$$

where $\widehat{U}_j$ is the specific internal energy of phase j and $\widehat{U}_R$ is the sediment (rock) specific internal energy.

The specific internal energy of the aqueous phase is calculated as follows:

$$\widehat{U}_A(T) = \widehat{H}_A(T) = \int_{T_0}^{T} \hat{C}_{pA} dT. \tag{10}$$

Neglecting pressure effects, $\widehat{U}_A$ is assumed equal to $\widehat{H}_A$, the specific enthalpy of water, and is only a function of temperature. The specific heat capacity of water, $\hat{C}_{pA}$, is determined empirically (Miller et al., 1976b).

For the free gas phase, methane is the predominant constituent, so the minimal presence of water vapor is neglected. The specific internal energy is therefore calculated as follows:

$$\widehat{U}_G(T, P_G) = \Delta\widehat{U}^0 + \widehat{U}^E_{T,P_G}, \tag{11a}$$

$$\widehat{U}_G(T, P_G) = \Delta\widehat{H}^0 - R(T - T_0) + \widehat{U}^E_{T,P_G}, \tag{11b}$$

$$\widehat{U}_G(T, P_G) = \int_{T_0}^{T} \hat{C}_{pG} dT + \Delta\widehat{H}^0 - R(T - T_0) + \widehat{U}^E_{T,P_G}, \tag{11c}$$

where T_0 is a reference temperature set to 273.15 K, $\Delta\widehat{U}^0$ and $\Delta\widehat{H}^0$ are the change in specific internal energy and enthalpy of methane as an ideal gas from temperature T_0 to T, R is the gas constant (8.314 J/mol·K), $\hat{C}_{pG}$ is the constant pressure specific heat capacity of methane, evaluated empirically (Tester and Modell, 1997), and $\widehat{U}^E_{T,P_G}$ is evaluated using the Peng-Robinson Equation of State (Tester and Modell, 1997). For the solid phases (sediment, hydrate, and ice) internal energy is considered only a function of temperature. Their specific internal energies are calculated as follows:

$$\widehat{U}_H(T) = \widehat{H}_H(T) = \widehat{H}_H^0 + \int_{T_0}^{T} \hat{C}_{pH} dT, \tag{12a}$$

$$\widehat{U}_I(T) = \widehat{H}_I(T) = -L_w + \int_{T_0}^{T} \hat{C}_{pI} dT, \tag{12b}$$

$$\widehat{U}_R(T) = \widehat{H}_R(T) = \int_{T_0}^{T} \hat{C}_{pR} dT, \tag{12c}$$

where $\widehat{H}_H^0$ includes the water enthalpy, gas enthalpy, and the formation enthalpy of hydrate at temperature T_0, and L_w is the latent heat of ice melting (Qin et al., 2003). Specific heat capacities for hydrate (Handa 1986) and ice (Fukusako and Yamada, 1993) are calculated empirically, while the specific heat capacity of the sediment phase is set to a constant.

Fluxes of mass for each component in both fluid phases are calculated as the sum of advection and diffusion components as follows:

$$F^i = \rho_G q_G x_G^i + \rho_A q_A x_A^i + J^i, \tag{13}$$

where q_G and q_A are the gas and Darcy velocities respectively and J^i is the diffusive flux of component i. Darcy velocities (volumetric flow per unit cross-sectional area normal to flow) of the aqueous and gas phases are calculated with the multiphase version of Darcy's Law (Lake, 1989):

$$q_j = -\frac{\mathbf{K} k_{rj}}{\mu_j} \cdot \left(\nabla P_j - \rho_j g\right), \tag{14}$$

where **K** is the absolute permeability tensor, k_{rj} is the relative permeability of phase j (a function of all phase saturations), μ_j is the viscosity of phase j, and g is the gravitational acceleration. Gas viscosity is calculated using an empirical equation (Selim and Sloan, 1989), and water viscosity is set at a constant 1 cp.

A scalar absolute permeability, K, is evaluated as a function of porosity via a power law model (Civan, 2001) as follows:

$$K = k_h k_0 \frac{\varphi}{\varphi_0} \left(\frac{\varphi(1-\varphi_0)}{\varphi_0(1-\varphi)}\right)^{2\beta}, \tag{15}$$

where φ is the sediment porosity, φ_0 is a reference porosity, k_0 is a reference seafloor permeability, β is an empirical parameter, and k_h modifies the sediment permeability as a function of hydrate saturation (Equation 2.17). In this formulation, the presence of hydrate changes the absolte permeability of the sediment, while relative permeabilities to aqueous and gas phases are calculated as a function the mobile phases present.

In general, sediment porosity is expressed as an exponentially decaying function of depth (Rubey and Hubbert, 1959):

$$\varphi = \varphi_\infty + (\varphi_0 - \varphi_\infty)\exp\left(-\frac{\sigma_e}{\sigma_\varphi}\right), \tag{16}$$

where φ_0 is the sediment porosity at the seafloor (typically around 70%), φ_∞ is the asymptotic porosity achieved (typically around 30%), σ_e is the vertical effective stress, and σ_φ is a characteristic stress constant. In the event that porosity data are available, empirical functions are applied to describe porosity variation with depth.

In the presence of pore-filling hydrate, permeability decreases with increasing gas hydrate saturation, so permeability is multiplied by kh following the formulation of Dai and Seol (2014):

$$k_h = \frac{(1-S_H)^3}{(1+2S_H)^2}. \tag{17}$$

Relative permeability to aqueous and gas phases are calculated using a modified Brooks-Corey model (Brooks and Corey, 1964; Lake, 1989):

$$k_{rG} = k_{rG}^0 (S_G^{e*})^{n_G}, \tag{18a}$$

$$k_{rA} = k_{rA}^0 (S_A^{e*})^{n_A}, \tag{18b}$$

where k_{rG} and k_{rA} are the gas and water relative permeabilities, respectively, k_{rG}^0 and k_{rA}^0 are the endpoint relative permeabilities of gas and water respectively, and n_G and n_A are exponents related to pore structure. The parameters S_G^{e*} and S_A^{e*} are the normalized gas and water saturations as follows:

$$S_G^{e*} = \frac{S_G^e - S_{Gr}^e}{1 - S_{Gr}^e - S_{Ar}^e}, \tag{19a}$$

$$S_A^{e*} = \frac{S_A^e - S_{Ar}^e}{1 - S_{Gr}^e - S_{Ar}^e}, \tag{19b}$$

where S_G^e and S_A^e are effective gas and water saturations as percentages of the pore space occupied by mobile phases, while S_{Gr}^e and S_{Ar}^e are correspondingly the effective residual gas and water saturations.

The diffusive flux of methane, water, and salt per unit volume are calculated according to Fick's first law (Bird et al., 2007; Webb, 1998):

$$J_j^i = -D_j^i \varphi \nabla x_j^i, \tag{20}$$

where D_j^i is the effective diffusion coefficient of component *i* in phase *j* in a porous medium. This coefficient is typically lower in porous media than in bulk conditions by up to an order of magnitude due to pore network tortuosity.

Flux of energy is calculated as the sum of convective and conductive heat transfer as follows:

$$F^e = \rho_G q_G \widehat{H}_G + \rho_A q_A \widehat{H}_A - \lambda \nabla T, \quad (21)$$

where $\widehat{H}_G$ and $\widehat{H}_A$ are the specific internal enthalpies of the gas and aqueous phases, respectively, and λ is the bulk effective thermal conductivity of the medium. The bulk effective thermal conductivity of the porous medium is calculated using a linear mixing rule (Quintard and Whitaker, 1995):

$$\lambda = (1 - \varphi)\lambda_R + \varphi \sum_j S_j \lambda_j, \quad (22)$$

where thermal conductivity of hydrate and sediment are assumed constant and thermal conductivities of gas (Yaws, 1995), water (Miller et al., 1976a), and ice (Fukusako and Yamada, 1993) are evaluated empirically.

This simulator employs a fully implicit finite volume difference method, which is versatile with respect to the coordinate system and dimension of the problems it can solve, as long as grid blocks are orthogonal. The time derivative is discretized using a backward Euler method, and the system is solved fully implicitly to ensure numerical stability. An upwinding scheme is employed to compute inter-block phase mobility.

The simulator uses a Newton-Raphson algorithm to solve the implicit system of nonlinear partial differential equations. The method proceeds iteratively by solving for ΔZ, the increment in primary variables, as follows:

$$\mathbf{J}\Delta Z = f, \quad (23)$$

where f is a vector of residuals of each governing equation and **J** is the Jacobian matrix of derivatives of each residual with respect to each primary variable, evaluated using a central difference scheme. The set of primary variables is solved for iteratively by using Matlab's linear solver library, and the Newton-Raphson method converges quadratically. Convergence is achieved when both the Euclidian norm and the infinity norm of the vector of primary variable increments becomes less than a prescribed tolerance ε. When convergence is achieved in under N_i maximum iterations, the simulation proceeds to the next time step with double the time step length (up to a prescribed maximum time step length). In the event that a solution is not reached in N_i iterations, the time step length is cut in half (down to a minimum time step length), and the solution search algorithm proceeds again at the current time step.

The primary variable switch method (PVSM) is used to track phase transitions during hydrate formation, dissolution, and dissociation (Pruess et al., 1999). Depending on the phase status of the system, this method changes the independent variables, or primary variables, that are solved for within a solution search iteration so as to minimize the number of independent equations that must be solved. For each phase status, up to three primary variables are selected from the set that includes gas, aqueous, ice, and hydrate saturations; temperature; gas pressure; and mass fraction of dissolved methane.

As an example, if a grid block is at three-phase equilibrium and contains aqueous, hydrate, and free gas phases, only one state variable is required to determine the thermodynamic state of the

block. Therefore, block temperature is solved as a primary variable. Hydrate, gas, and aqueous saturations must add to unity, so only two phase saturations, hydrate and aqueous, are solved as primary variables. Contrastingly, if the grid block in question only contains hydrate and aqueous phases in the pore space, two state variables, pressure and temperature, are required to be solved for in order to determine the thermodynamic state of the grid block. Hydrate and aqueous phases add to unity, so the third primary variable is chosen to be hydrate saturation.

Gas phase pressure is solved as a primary variable, and aqueous phase pressure is always calculated by subtracting capillary pressure from the gas phase pressure. When gas saturation is zero, its corresponding pressure is calculated as a theoretical gas pressure if a gas phase were to exist in equilibrium with the aqueous phase. If dissolved methane exists at solubility in an aqueous phase, then it will be in equilibrium with a hypothetical free gas phase according to Henry's Law, so the gas phase pressure (whether or not gas exists) is always used in calculating aqueous methane solubility.

In the following work capillary pressure is formulated as a function of effective pore radius, or the smallest pore radius occupied by a given nonwetting phase (hydrate or free gas). Gas hydrate and free gas are both assumed to be completely nonwetting phases, filling the pore space without touching grain surfaces. These phases are assumed to grow out of solution in spherical configuration, and therefore the pores are also assumed to be spherical for the purposes of capillary pressure calculation and phase boundary adjustments owing to the Gibbs-Thomson effect, which is described in the next section.

2.2 Capillary controls on hydrate and free gas growth in pores

2.2.1 Two-phase (hydrate-aqueous and gas-aqueous) systems

Free gas or gas hydrate phase formation occurs when the concentration of methane dissolved in pore water exceeds its solubility at a specified pressure, temperature, and pore water salinity. In our simulations, we additionally incorporate the impact of pore curvature on phase stability. We consider the hydrate phase to be nonwetting with respect to grain surfaces in a water-wet porous medium, assuming the hydrate-sediment grain interfacial energy is large relative to the liquid water-sediment interfacial energy. This non-wetting behavior has been observed in laboratory imaging (Kerkar et al., 2014; Chaouachi et al., 2015). This assumption implies that hydrate forming out of aqueous solution must grow entirely within sediment pore space and that it does not touch sediment grain boundaries.

In sufficiently large pores (greater than a few microns in diameter), hydrate crystal growth can occur in pore fluid as if it were in bulk solution because its surface area to volume ratio is sufficiently low that changes in bulk free energy caused by the curvature of the hydrate-water interface is negligible. However, as pore size decreases, the volume of a growing hydrate mass within that pore must correspondingly decrease. As the volume of a spherical mass decreases, its surface area to volume ratio increases. Known as the Gibbs-Thomson effect, previous studies have derived equations predicting the three-phase equilibrium (Clennell et al., 1999; Henry et al., 1999) and corresponding solubility of methane (Sun and Duan, 2007) in pore fluid as it changes due to small pore sizes. Small pores generally require a greater driving force to form hydrate as

compared to bulk conditions, and this results in the need for a higher pressure, subcooling, or a greater supersaturation of methane in pore fluid before hydrate growth can proceed. Assuming spherical pores, we employ the Gibbs-Thomson equation to describe the three-phase (gas-water-hydrate) equilibrium temperature depression required to form hydrate at a given pressure (Anderson et al., 2009):

$$\Delta T_m = \frac{2T_{mb}\sigma_{hw}\cos\theta_{hs}}{H_f\rho_H r_{eh}}, \tag{24}$$

where T_{mb} is the bulk melting temperature of methane hydrate in water, θ_{hs} is the contact angle between hydrate and the pore wall (assumed to be 180°), H_f is the latent heat of fusion for hydrate, ρ_H is the density of solid hydrate, r_{eh} is the smallest, or effective, pore radius defining the effective curvature of the hydrate phase, and σ_{hw} is the hydrate-water interfacial energy (0.027 J/m^2) (Clennell et al., 1999). For the purposes of this study, we neglect any hysteresis during formation and dissociation.

For a given in situ temperature T_0 within the pore space, the temperature is therefore adjusted when calculating the hydrate freezing pressure as follows before being used to calculate the corresponding three-phase equilibrium pressure:

$$T = T_0\left(1 - \frac{2\sigma_{hw}\cos\theta_{hs}}{H_f\rho_H r_{eh}}\right). \tag{25}$$

For a given pore water temperature in a hydrate-water system, the phase boundary pressure shifts to higher pressure in Equation 25 if θ_{hs} is 180° (Fig. 5a). This effect is amplified at higher temperatures. Since at a given temperature the 3-phase equilibrium boundary pressure controls methane solubility in a hydrate-water system, methane solubility is effectively enhanced as pore size decreases.

Similarly, assuming the free gas phase also does not wet the grain surfaces in a water wet medium, forming a free gas phase in pores requires a capillary pressure (the difference between gas pressure and water pressure) to maintain a gas-water interface in those pores; this pressure increases with increasing pore curvature. When hydrate and gas both occupy small pores of various sizes, end-member scenarios of purely hydrate in small pores and purely gas in small pores thus essentially constitute bounds on the 3- phase equilibrium boundary, though the actual pore size occupied by either phase is determined by methane availability.

Since free gas and water are considered immiscible fluid phases, a curved interface between gas and water in a porous medium exists and is supported by a capillary pressure. Assuming spherical pores, this capillary pressure is described using the Washburn equation as follows:

$$P_{cgw} = -\frac{2\sigma_{gw}\cos\theta_{gs}}{r_{eg}}, \tag{26}$$

where θ_{gs} is the contact angle between gas and the pore wall (assumed to be 180°), and r_{eg} is the smallest pore radius in which gas is present. The gas phase pressure, P_g, is defined as the sum of

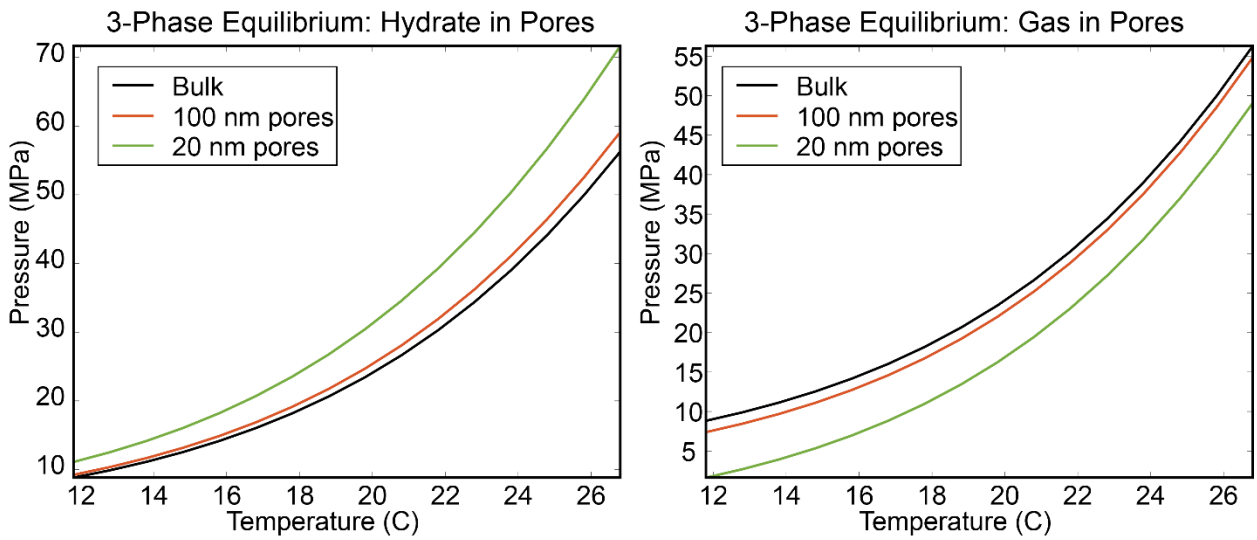

Figure 5. (a) Hydrate presence in small pores shifts the 3-phase equilibrium boundary to higher gas pressures and lower temperatures than bulk equilibrium, while (b) gas presence in small pores can be understood as effectively shifting the boundary to lower pressures and higher temperatures.

the water pressure, P_w, and the capillary pressure, P_{cgw}, and σ_{gw} is the gas-water interfacial energy (0.072 J/m^2 for methane in water) (Clennell et al., 1999).

From Henry's law, it follows that methane solubility is enhanced as a function of capillary pressure (Liu and Flemings, 2011):

$$\frac{\Delta C_{LG}}{C_{LG0}} \approx \frac{P_{cgw}}{P_w} = -\frac{2\sigma_{gw}\cos\theta_{gs}}{r_{eg}P_w}. \tag{27}$$

2.2.2 Three-phase (hydrate-gas-aqueous) systems

Some geophysical and numerical studies have proposed the existence of a 3-phase stability region near the bulk base of the MHSZ (BHSZ) to explain the appearance of a free gas phase at shallower depths than predicted by bulk 3-phase equilibrium thermodynamics (Liu and Flemings, 2011). Most agree that a region of three-phase stability is possible by invoking the presence of either a pore size distribution in hydrate- and gas-bearing sediments, the presence of different gases in the hydrate phase besides methane (Paganoni et al., 2016), or significant local gradients in salinity owing to salt exclusion during hydrate formation (though the latter is a transient process; i.e., Liu and Flemings, 2006). This work expands upon the formulation of Liu and Flemings (2011) by simulating the coupled flow mechanics of phase transitioning in a methane-constrained system. Additionally, we describe three-phase coexistence in pore space as generally being controlled by the effective curvatures of hydrate and free gas phases.

The logic of simulating a porous medium at hydrate-aqueous-free gas equilibrium is as follows (Fig. 6):

1. If, as established in §2.2.1, dissolved methane concentrations in equilibrium with gas hydrate are enhanced in small pores, then pore curvature (as a proxy for hydrate phase curvature) can be directly mapped to effective aqueous methane solubility.

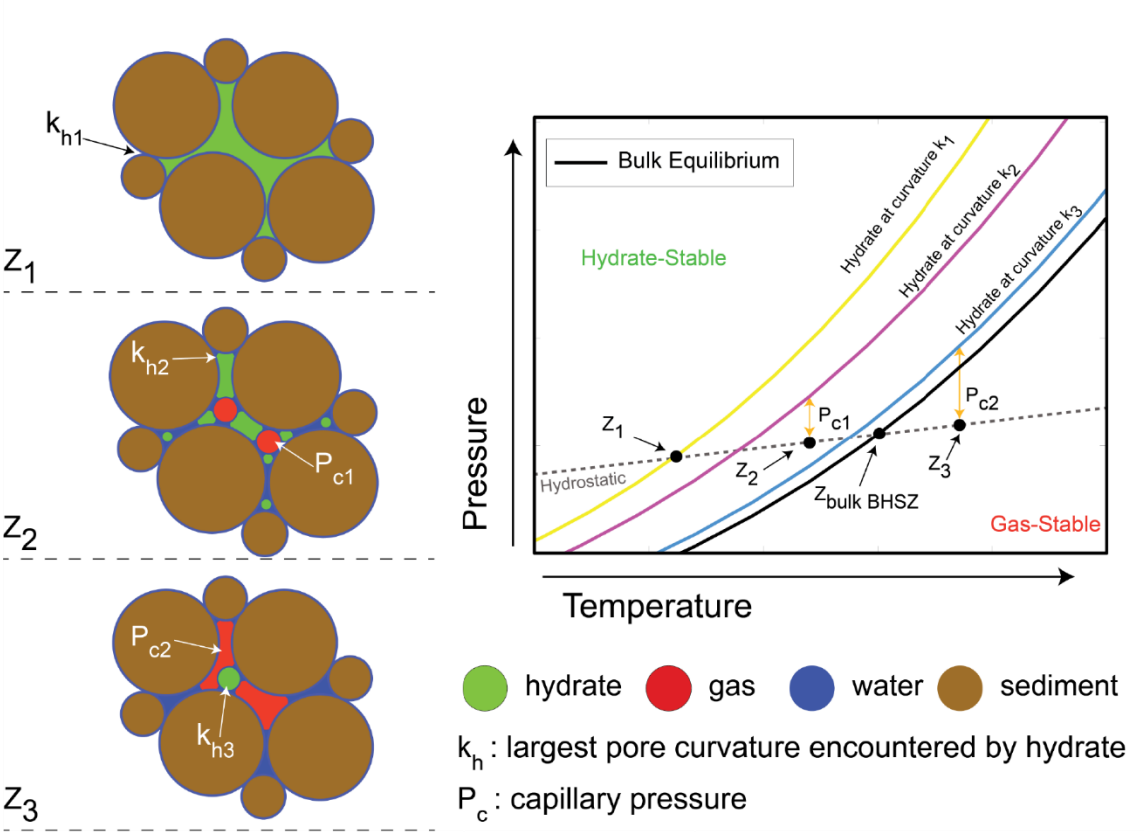

Figure 6. A schematic of the progression of the three-phase stability region in a general porous medium. Three-phase equilibrium is determined by the gas pressure, which is a hypothetical bulk gas pressure in hydrate-water systems and differs from water pressure by the capillary pressure when gas is present. When hydrate exists in small pores, gas can form above the bulk BHSZ, and when gas exists in small pores hydrate can exist below the bulk BHSZ.

2. When methane hydrate, free gas, and dissolved methane exist in 3-phase equilibrium, dissolved methane concentration is uniform throughout all pore sizes.
3. Dissolved methane concentration is a function of methane partial pressure in the free gas phase, which is a function of capillary pressure.
4. Since gas pressure controls methane solubility at 3-phase equilibrium, and since solubility can be mapped to hydrate phase curvature, the gas pressure controls the curvature of both the free gas and the hydrate phases.

When sediment containing gas hydrate is buried to higher pressure and temperature through the MHSZ, it eventually approaches the phase boundary. The extent to which this boundary is shifted above bulk conditions is determined by the largest curvature of the hydrate phase. Note that this also depends on the methane abundance inthe system, as greater methane abundance will result

in larger hydrate saturation, causing hydrate to be present in smaller pores. Water pressure and temperature both increase as a system is buried (dashed line in Fig. 6): water pressure increases hydrostatically (in the absence of any overpressure) and temperature increases along the

geothermal gradient. Therefore in this schematic, the system first reaches a 3-phase equilibrium depth, z_1, above the bulk BHSZ because hydrate exists in pores at a curvature k_1.

When the system is buried past this point, to z_2, the pressure and temperature of the system pass the original phase boundary and some hydrate must convert to free gas. This free gas has an associated capillary pressure, P_{c1}. Since depth z_2 is still above the bulk BHSZ, hydrate must still be present if free gas is present. When gas grows here, hydrate dissolves in pores with the largest curvature such that its effective curvature decreases. This in turn lowers the phase boundary until it converges, at an effective curvature k_2, with the gas pressure (hydrostatic pressure plus P_{c1}). The formulation of this simulator assumes the gas pressure determines methane solubility when gas is present; therefore in a 3-phase system with free gas present the solubility of both free gas and hydrate are determined by gas pressure through Henry's Law. This assumption could certainly be improved upon with experimental data in future work.

The effective curvature of the hydrate phase decreases with progressive burial while the effective curvature of the gas phase correspondingly increases. At depth z_3, the gas phase curvature is higher than before because the capillary pressure, P_{c2}, required to sustain a hydrate phase at curvature k_3, is higher than the capillary pressure required to maintain hydrate at curvature k_2 at depth z_2.

This process is inherently limited by the availability of methane, which is why simulating the evolution of a hydrate system transitioning from hydrate-stable to gas stable should incorporate fully coupled methane and water mass transport dynamics, as has not been performed to date. Methane availability constraints can be understood by examining aqueous methane concentrations in a hydrate system as a function of depth (Fig. 7).

When sediments containing gas hydrate are buried through the MHSZ, methane solubility continuously increases with burial depth because methane solubility in a hydrate-water system is a stronger function of temperature than pressure. Generally, in the absence of any external methane sources, the burial of a hydrate mass results in thermodynamic disequilibrium: hydrate is present in pore space, but the concentration of methane in pore fluid is below solubility, meaning hydrate is unfavorable in the smallest pore. To re-equilibrate, methane is added to the pore fluid via hydrate dissolution, which increases dissolved methane concentration at the expense of hydrate saturation. If hydrate is not present in sufficient quantities to supply the required amount of methane, all of the hydrate will be driven to dissolve.

If the system is at bulk conditions (Fig. 7a), methane concentration in equilibrium with hydrate is fixed at bulk methane solubility (circle A). If system is then buried, hydrate and its pore fluid are in disequilibrium (dashed circle B). To resolve this imbalance, hydrate dissolves, adding methane to the dissolved phase until thermodynamic equilibrium is reached (circle C). Eventually, the system will be buried past the bulk phase boundary at the BHSZ (dashed circle D). At this point all hydrate remaining will dissociate into free gas and water (circle E). If enough free gas is present beneath the BHSZ, buoyant gas can migrate upward (Fig. 7b). If the gas phase moves past the phase boundary (dashed circle C), hydrate becomes more stable than gas, so the system is driven toward hydrate formation at the expense of all gas present.

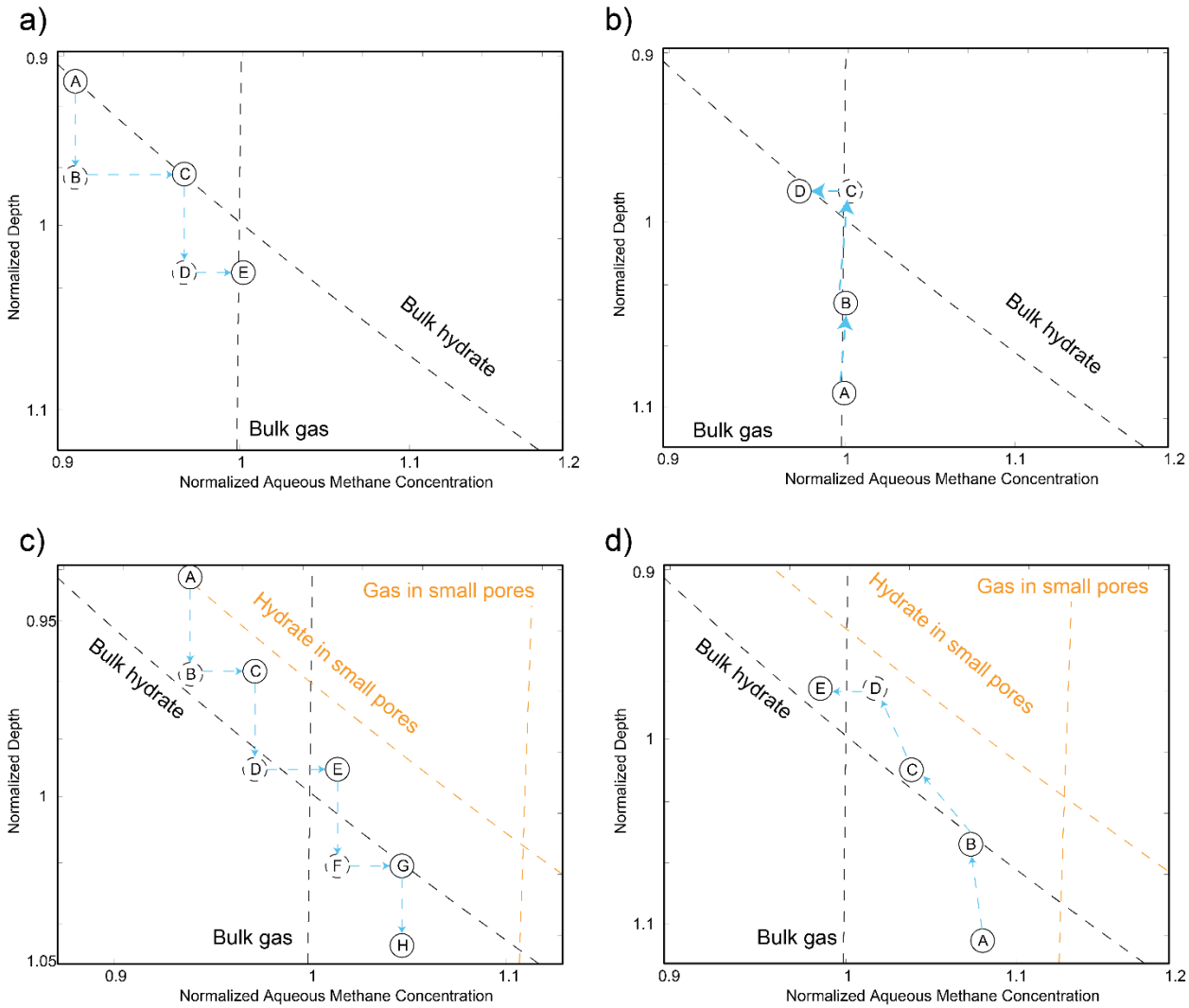

Figure 7. The evolution of aqueous methane concentration as (a) hydrate is buried past the BHSZ at bulk conditions, (b) gas migrates upward past the BHSZ at bulk conditions, (c) hydrate present in a pore size distribution is buried through the 3-phase zone, and (d) gas migrates upward in a pore size distribution from beneath the 3-phase zone.

In reality, the systems depicted in Figures 7a and 7b occur in tandem: burial of a hydrate system past the BHSZ produces free gas, which then can potentially migrate back upward. But at bulk equilibrium, the transition from hydrate to gas occurs abruptly at one specific depth. All methane held as hydrate here converts instantaneously into gas (neglecting hydrate formation or dissociation kinetics on geologic timespans), and all of the excess gas above the critical gas saturation will flow back upward to accumulate at the BHSZ until hydrate saturations become high enough to divert fluid flow elsewhere.

If, instead, methane solubility in water is considered a function of nonwetting phase saturation via a pore size distribution, a transition region can exist in which gas, hydrate, and water coexist in pores of different sizes at any given depth. Considering hydrate present in a distribution of pore sizes at a given effective curvature, when the system is buried (to dashed circle B) hydrate

will be in disequilibrium with dissolved methane and must therefore dissolve. Lowering hydrate saturation lowers the effective curvature of the hydrate phase, which lowers the effective solubility of methane. Thus, the dissolved methane concentration and the effective methane solubility in the smallest pores occupied by hydrate eventually converge (circle C) at a methane concentration lower than that which would have been required for hydrate in pores at circle A because hydrate is no longer present in those pores. This process is repeated (dashed circle D) until the system crosses the phase boundary (circle E). At this point, gas is the preferred phase for growth. As gas forms in large pores and then in smaller pores, the gas-water capillary pressure increases with increasing gas saturation. The capillary pressure and the 3-phase equilibrium pressure converge to generate a distribution of gas and hydrate at 3- phase equilibrium.

When buoyant gas migrates upward in sediment with a distribution of pore sizes (Fig. 7d), once it crosses the phase boundary methane partitions into the hydrate phase. The free gas phase that remains continues migrating upward where hydrate becomes more stable and a greater proportion of methane partitions into the hydrate phase. This process continues until the free gas phase is no longer mobile.

The exact mechanics of the coexistence of hydrate, water, and gas in pores have not yet been fully explored experimentally; however, thermodynamic equilibrium requires that hydrate present in pores must dissociate into gas once it is buried to depths where gas is the preferred phase over hydrate. Since the mechanics of hydrate-to-gas transitioning in sediments characterized by pore size distributions are not well understood, we make a number of assumptions that ensure convergence to a unique numerical solution in the following simulations and compare their results. What we will demonstrate, however, is that the hydrate-gas-water system cannot be treated like a typical multiphase fluid system because the presence of each nonwetting phase is coupled to the how the other phase is distributed.

First, we assume that either phase has equal affinity for the largest pores because both hydrate and gas would prefer to occupy these pores when 3 phases are stable (Liu and Flemings, 2011). This means that when a two-phase system transitions to a 3-phase system, the new phase evenly partitions the occupied pore space with the other nonwetting phase. In the case of hydrate dissociation and free gas formation, this means that if hydrate is present in small pores and a gas phase is stable in large pores, hydrate will dissociate in half of the large pores that are available to gas, and gas will form in those pores. If it were stipulated that gas were the only stable phase in the largest pores, as one might expect since the gas-water interfacial energy is higher than the hydrate-water interfacial energy, infinitesimally small amounts of hydrate in the smallest pores would exert significant influence on the 3-phase equilibrium boundary and result in a significant discontinuity (explained below). Therefore, the following equations represent the conditions imposed to determine the pore sizes that govern capillary effects on either the gas or hydrate phase following Liu and Flemings (2011). For a given pore size distribution where the effective pore radius, re occupied by a given phase is a function of the saturation of that phase (the derivation of a synthetic pore size distribution is described in Section 2.3):

$$r_g = \begin{cases} r_e(S_g + S_h), S_g > S_h \\ r_e(2S_g), S_g < S_h \end{cases}, \tag{28a}$$

$$r_h = \begin{cases} r_e(S_h + S_g), S_h > S_g \\ r_e(2S_h), S_h < S_g \end{cases}, \tag{28b}$$

where r_g is the effective pore radius of the gas phase and rh is the effective pore radius of the hydrate phase. In a two-phase system, both conditions collapse to the same expression for effective pore radius as a function of a single nonwetting phase saturation (gas or hydrate).

Now we consider why gas and hydrate must co-occupy the large pore space to some degree (though not necessarily 50/50). To prove this point we will consider a situation where the large pore space can only be occupied by one phase. If we assume that the hydrate phase always occupies the smallest pores because the hydrate-water interfacial energy is lower than the gas-water interfacial energy, then for a given pore size distribution, these conditions require the following:

$$r_h = r_e(S_h + S_g), \tag{29a}$$

$$r_g = r_e(S_g). \tag{29b}$$

Unfortunately, as formulated, this condition contains a non-unique discontinuity as r_g approaches r_h. Consider pore space filled with hydrate to a smallest pore r_{min}. When the system is buried to a point where gas becomes stable in the largest pores, methane from the hydrate phase will convert into the gas phase, and gas will enter successively smaller pores. Through this process, the effective pore radii occupied by hydrate and gas will converge until all hydrate disappears. At this point, the phase boundary would instantly jump to lower pressure and higher temperature since hydrate would no longer exist to push the phase boundary in the opposing direction. The gas pressure would be too high to maintain the gas saturation in the pore space, and hydrate would need to form at bulk conditions (or the largest pores). But it would not be able to do so if it were stipulated that it could only be in pores smaller than gas.

This therefore proves that in addition to wetting behavior, phase stability also dictates the size of the pores each phase can occupy. Or, more accurately, the effective pore size as implemented in these simulations should be thought of more as an effective curvature: hydrate and gas can likely occupy the same pores at 3-phase equilibrium but at different effective curvatures. Thermodynamic phase stability dictates that effective hydrate phase curvature will decrease smoothly with depth while effective gas phase curvature will correspondingly increase with depth. The 50/50 phase co-occupancy rule for phase partitioning in the largest pores ensures that the effective pore radii at given hydrate and gas saturations are uniquely defined (the system is non-hysteretic). Although the assumption of hydrate-gas co-occupancy in large pores adequately captures the numerical requirement that each nonwetting phase exhibit a smooth gradation in curvature, the specific phase partitioning assumption is not backed by experimental data. Phase partitioning in the 3-phase zone should be explored experimentally in porous media to get a more accurate picture of how the expression of a 3-phase zone could vary across different geologic settings.

Next, we assume that the largest pores of my sediments are generally well connected. Therefore, in a scenario in which gas begins to form where hydrate is already present, gas mobility is not affected by the presence of hydrate in small pores because gas is only present and mobile in the large pores. Thus, although absolute permeability is expressed as a function of hydrate saturation, relative permeability is independent of the presence of hydrate in small pores. In this work, relative permeability is expressed using a Brooks-Corey model taking into account each mobile phase as a fraction of the total amount of fluid in the pore space (Brooks and Corey, 1964). Therefore, for a given gas saturation, an increasing hydrate saturation would decrease the aqueous phase saturation and thus increase the percentage of gas relative to the mobile phases, which would increase its mobility (Amyx et al., 1960). This is consistent with the idea that, since a gas phase fills the largest and best-connected pores when hydrate is stable in small ones, its mobility is generally not dependent on the size of the pores it occupies. Detailed gas relative permeability experiments in hydrate-bearing sediments could provide more insight into this assumption.

2.3 Parameterizing the subsurface

This study hypothesizes that the interaction between inherent lithologic heterogeneities and the mechanisms of methane migration in hydrate-bearing environments together control the dynamics of gas hydrate occurrence and distribution in the pore space of buried sediments. The work here proposes a number of advancements in how heterogeneity is parameterized that have not yet been widely implemented in gas hydrate reservoir simulators. These in include describing sediment pore space as containing distributions of pore sizes, implementing depth-dependent local sourcing of methane via microbial methanogenesis, tailored reference frames for exploring different migration phenomena, and integrating interpreted seismic data with discretized hydrate reservoirs.

2.3.1 Parameterizing pore size distributions

In a porous medium containing a distribution of pore sizes, the nonwetting free gas, hydrate, and ice phases will preferentially fill large pores first before filling smaller pores, which correspondingly results in an effective solubility increase with decreasing pore size (Liu and Flemings, 2011). Therefore, as the sediment pore space fills with a nonwetting phase, progressively larger amounts of dissolved methane are required in order to grow the nonwetting phase into successively smaller pores.

As the radius of a spherical pore decreases, its curvature correspondingly increases. This work assumes that as pore curvature increases, interfacial curvature of the nonwetting phase contained within a pore also increases. To incorporate the effect of changing interfacial curvature with changing pore size, we describe an effective pore radius that decreases with increasing nonwetting phase saturation. We approximate a pore size distribution with a lognormal distribution that has a median pore radius r_m and standard deviation τ_r; we then consider how the effective pore radius influencing three-phase equilibrium in a porous medium changes as a function of nonwetting phase saturation. First, we define a lognormal cumulative distribution function in terms of incremental (effective) pore radius, r_e, total pore volume, V_{tot}, and cumulative volume, V, in pores smaller than r_e:

$$\frac{V}{V_{tot}} = 0.5\left(1 + \mathrm{erf}\left(\frac{\ln(r_e)-\mu}{\sqrt{2}\tau}\right)\right), \tag{30a}$$

$$\mu = \ln\left(\frac{r_m}{\sqrt{1+\frac{\tau_r^2}{r_m^2}}}\right), \tag{30b}$$

$$\tau = \sqrt{\ln\left(1 + \frac{\tau_r^2}{r_m^2}\right)}, \tag{30c}$$

where μ is the location parameter and τ is the scale parameter of the distribution.

As a nonwetting phase starts forming (where effective curvature is the lowest), the largest pores will fill with that phase first. This process is similar to drainage of a wetting fluid in a porous medium by a nonwetting fluid. Equation 8 therefore represents the volume fraction of wetting phase-occupied pore space whose pore radius is less than or equal to r_e (neglecting the volume of thin water films in the larger pores). If water, gas, ice, and hydrate can fill the pore space as nonwetting phases, Equation 8 can be rewritten as follows:

$$1 - S_h - S_g - S_I = 0.5\left(1 + \mathrm{erf}\left(\frac{\ln(r_e)-\mu}{\sqrt{2}\tau}\right)\right), \tag{31}$$

where S_h is saturation of gas hydrate (the fraction of pore space occupied by gas hydrate), S_g is the free gas saturation, and S_I is the ice saturation. Solving for effective pore radius as a function of nonwetting phase saturations, Equation 31 can be rearranged as follows:

$$r_e = \exp\left(\sqrt{2}\tau\mathrm{erf}^{-1}\left(1 - 2S_h - 2S_g - 2S_I\right) + \mu\right), \tag{32}$$

where r_e is the effective pore radius governing methane solubility of the smallest pore in which a nonwetting phase can form (Fig. 8). In the present work, this effective pore radius is used both in the Gibbs-Thomson equation and in gas-liquid capillary pressure calculations to describe the evolution of the three-phase equilibrium pressure with changing hydrate and gas saturations in the system. This treatment approximates the effect of increasing gas hydrate saturation on methane solubility described by Rempel (2011).

In sediments characterized by gradational lithology or an otherwise non-binary (sand or clay) designation, the effective pore radius is scaled to account for fines fraction and is re-expressed as follows:

$$r_e(S_{nw}) = f_f\left(r_f\right) + \left(1 - f_f\right)\exp\left(\sqrt{2}\tau\mathrm{erf}^{-1}(1 - 2S_{nw}) + \mu\right), \tag{33}$$

where f_f is a fines fraction ranging from 0 to 1 and r_f is the pore radius of the fine-grained

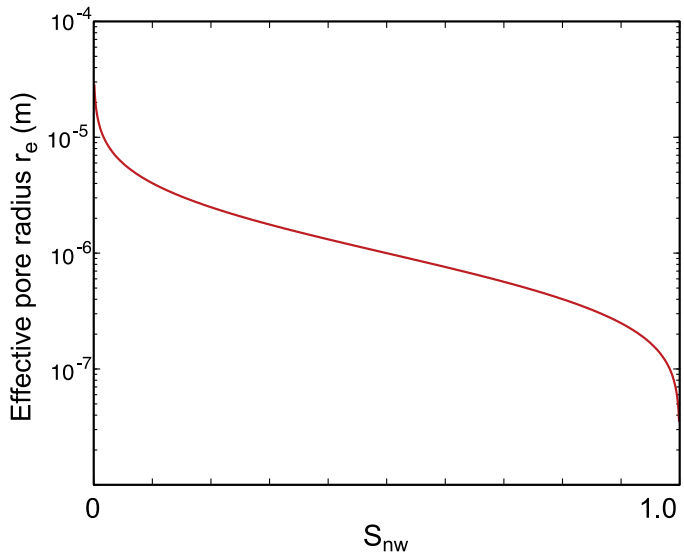

Figure 8. The synthetic pore size distribution used in this work, where the radius of the smallest pore occupied by a nonwetting phase decreases with increasing nonwetting phase saturation.

material. This formulation assumes that the volume of sediment being considered is a mixture of sands and fines. A given grid block could either be purely mixed media (Daigle and Reece, 2015) or contain fine-scale layers beneath the resolution of the grid block that are bulk-averaged into f_f. This is a simple linear mixing rule and could certainly be improved upon in future work.

In a pore size distribution, 3-phase equilibrium can exist across a range of pressures and temperatures as the two non-wetting phases can occupy different parts of the pores space. This is particularly relevant near the BHSZ, where hydrate transitions into free gas and methane recycling can potentially occur. This means that methane in smallest pore occupied by gas must be in thermodynamic equilibrium with dissolved methane and methane in the hydrate phase in the smallest pore occupied by hydrate. The condition of hydrate-gas co-occupancy in the largest pores constrains these pore radii to unique configurations as simple functions of hydrate and gas saturation as follows:

$$r_{eh}(S_h, S_g) = \exp\left(\sqrt{2}\tau \mathrm{erf}^{-1}(1 - 2S_h^*) + \mu\right), \tag{34a}$$

$$r_{eg}(S_h, S_g) = \exp\left(\sqrt{2}\tau \mathrm{erf}^{-1}(1 - 2S_g^*) + \mu\right), \tag{34b}$$

$$S_h^* = \begin{cases} 2S_h, S_h < S_g \\ S_h + S_g, S_h \geq S_g \end{cases}, \tag{34c}$$

$$S_g^* = \begin{cases} 2S_g, S_g < S_h \\ S_h + S_g, S_g \geq S_h \end{cases}, \tag{34d}$$

where r_{eh} is the effective pore radius occupied by hydrate, and r_{eg} is the effective pore radius occupied by gas.

In the current work, simulations are performed within and immediately below the MHSZ, and temperatures remain above the freezing temperature of water, so ice is never a stable phase. Therefore, S_I in Equations 11 and 12 is always equal to 0. We apply this process only to silty/sandy reservoirs in the simulation, where the assumption of pore-filling gas hydrate morphology is expected to be valid. We describe clay layers by a single pore size and ignore pore size distribution effects in the clay layers because gas hydrate is not typically observed in a pore-filling habit in clay sediments. Rather, hydrate tends to fill fracture or vein networks in these sediments, and over a regional scale, gas hydrate saturations as a percentage of clay pore space tend to be small (around 5%; Cook et al., 2014).

2.3.2 Microbial methanogenesis

In the shallow subsurface of many marine environments, beneath the sulfate reduction zone microbes known as methanogens convert organic material that has been deposited on the seafloor into methane (Claypool and Kaplan, 1974). This constitutes a major source of methane in hydrate-bearing sediments in addition to methane derived through thermogenic processes. Methanogens mainly act in organic-rich, clayey sediments and are inactive in sandy units because those units typically lack organic matter (Claypool and Kaplan, 1974; Hedges and Keil, 1995; Waseda, 1998; Pohlman et al., 2009). As the organic matter in the clayey layers is consumed by methanogens, less organic matter remains and therefore less methane is produced over time, giving rise to an exponential decay in organic carbon content with time.

A dynamic system therefore typically exists with respect to methanogenesis in marine gas hydrate systems. At steady state, the microbial methane production rate can be expressed as a decreasing function of depth as organic matter is consumed. Since the sediments in which methanogenesis primarily takes place (fine-grained clayey material) can hold more aqueous methane in solution than the coarse-grained sand layers due to their small pore sizes, diffusive gradients typically exist between clayey and sandy layers (Malinverno, 2010; Rempel, 2011). This drives a flux of dissolved methane diffusively from finegrained clays to coarse-grained sands, which promotes hydrate growth in the coarse-grained layers due to short migration of methane.

Steady state methane generation due to microbial methanogenesis is implemented following the formulation of Malinverno (2010) as follows:

$$q(z) = k_\alpha \lambda_{meth} \alpha_{SMT} \exp\left(-\frac{\lambda_{meth}}{\omega}[z - z_{SMT}]\right), \tag{35}$$

where $q(z)$ is a depth-varying source of methane into the pore space, k_α is a conversion factor from metabolizable organic carbon mass fraction to dissolved methane concentration, λ_{meth} is the reaction rate of microbial methanogenesis, α_{SMT} is the mass fraction of metabolizable organic carbon at the sulfate-methane transition (SMT), ω is the sedimentation rate, and z_{SMT} is the depth below seafloor of the SMT. To justify a steady state methanogenesis assumption, the domain simply assumes that methanogens are already present in organic-rich strata throughout the sediment column as an initia lcondition. In sediments characterized by gradational lithology, this methanogenesis source is re-expressed as follows:

$$q(z) = f_f k_\alpha \lambda_{meth} \alpha_{SMT} \exp\left(-\frac{\lambda_{meth}}{\omega}[z - z_{SMT}]\right), \quad (36)$$

where f_f is a fines fraction and is applied the same way as in Equation 33.

2.3.3 Simulation reference frames

One- and two-dimensional simulations were performed on a small scale at high resolution to assess the impact of methane diffusion and methane recycling on gas hydrate distributions within and immediately surrounding coarse-grained layers buried through the MHSZ amidst clayey background material. To achieve this resolution over the entire depth of the MHSZ, we adopt a Lagrangian reference frame: boundary conditions change through time in the simulation to reflect increasing pressure and temperature with burial.

The 1-D simulation control volume is depicted in Figure 9. In these simulations, a compaction-driven fluid flux boundary condition varies with time at the bottom of the domain. Compaction reduces porosity with burial and moves fluid upward relative to the sediment grains; this effect diminishes as the change in porosity of the system with burial approaches zero (Berner, 1980). This stands in contrast to a fixed Eulerian reference frame (as in the 3-D simulations performed here), in which compaction-driven fluid flow is downward when the reference frame is fixed at the seafloor (e.g. Bhatnagar et al. (2007); Frederick and Buffett (2011)). The top of the domain is kept at a constant pressure corresponding to hydrostatic pressure at the depth of the boundary. While this pressure may not be exactly hydrostatic (if fluid is moving upward above the domain), the magnitude of any overpressure in this control volume due to compaction flux has a negligible impact on methane solubility throughout the domain.

Boundary temperatures are fixed along a geothermal gradient. The simulation boundaries are placed sufficiently far from the sand such that hydrate growth in the sand is separated from hydrate in clays by hydrate-free zones (HFZ). Initially, methane is absent from the system at the SMT, and the methane concentrations on the top and bottom boundaries are set equal to the methane concentrations in their respective adjacent grid blocks with the addition of dissolved methane due to methanogenesis on the boundaries.

In 2-D, the Lagrangian simulation domain is used for diffusion simulations and is discretized into an array of right rhombic prisms; the gravity vector is rotated to simulate a dipping reservoir unit (Fig. 10a). This is important because in a rectangular grid system oriented orthogonal to gravity, the edge of a dipping sand must be described by a discrete step function, across which diffusion can act laterally and vertically. When the scale of grid discretization is on a similar order of magnitude to the thickness of the sand itself, a jagged sand edge could yield unwanted methane diffusion parallel to the sand surface.

Boundary conditions are formulated in the same way as described for 1-D simulations. Also as in 1-D, the system is initially devoid of methane. On the top and bottom boundaries, methane concentrations are formulated as functions of time in the same way as in 1-D simulations: at each time step, the methane concentration on each boundary is set to the methane concentration in the grid block adjacent to the boundary at the previous time step plus the addition of methane due to

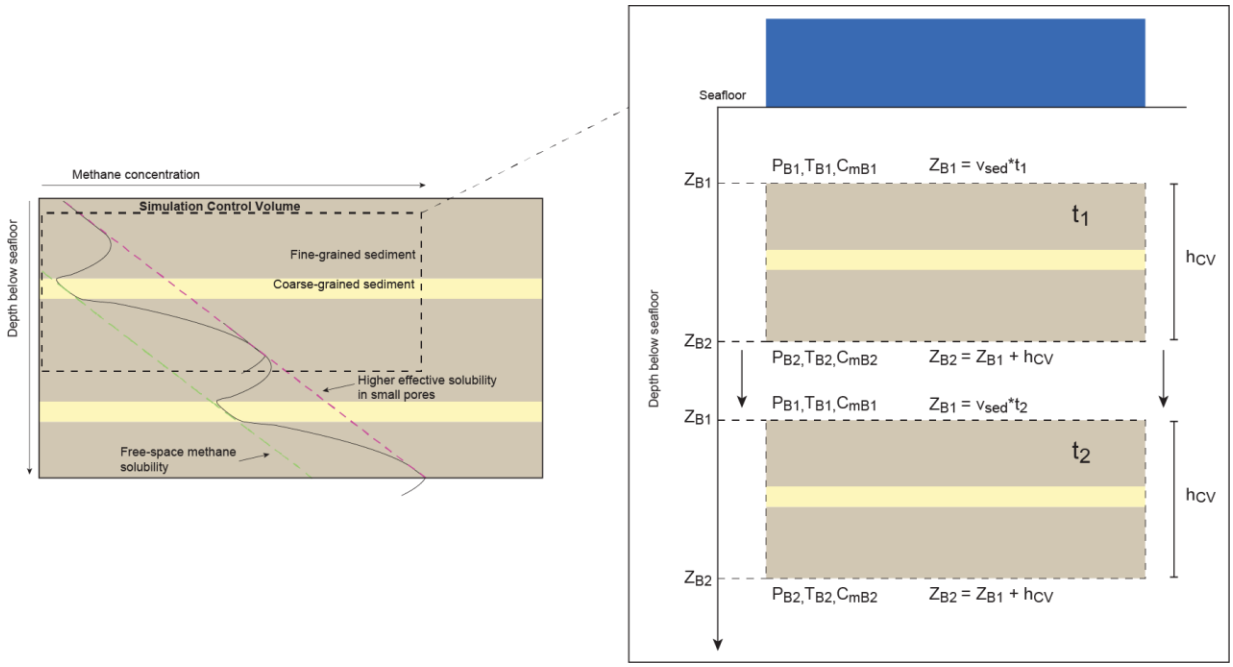

Figure 10. A fully developed methane concentration profile (left-hand panel) in a repeating sequence of alternating fine- and coarse-grained sediments with the free space methane solubility (dashed green line) and clay layer effective methane solubility (dashed magenta line) superimposed. The control volume in 1-D centers around a sand layer that is buried over time. Boundary conditions change with time (right-hand panel). Modified from Nole et al (2017).

methanogenesis on the boundary. On the sides of the domain, no flux boundary conditions are prescribed for methane concentrations.

Two-dimensional flow focusing simulations and 3-D diffusion simulations at the Terrebonne Basin are performed in an Eulerian reference frame with static boundary conditions; as coarse-grained sand layers are buried through the domain, new fine-grained material is deposited on top (Fig. 10b). The top boundary is set at seafloor hydrostatic pressure, the bottom boundary condition is that of constant advective compaction flux, and constant temperature boundary conditions on the top and bottom of the domain are defined by the geothermal gradient. As initial conditions, methane concentrations and methane hydrate saturations throughout the domain are set to zero.

One- and two-dimensional simulations are limited in that they cannot describe regional-scale gas hydrate distribution patterns; 1-D simulations illustrate hydrate distributions within a sand layer itself, while 2-D simulations demonstrate how effective methane solubility differences and flow fields in multiple directions affect average hydrate saturations in and around a reservoir layer. The benefit of 1-D and 2-D simulations is that they provide results at a resolution not possible in 3-D simulations due to computational limitations. Three-dimensional simulations are therefore not able to resolve hydrate-free zones immediately surrounding sand layers; nor can they depict gas hydrate distributions within individual sands. They do, however, illustrate regional gas hydrate distribution trends across multiple dipping, non-planar sands.

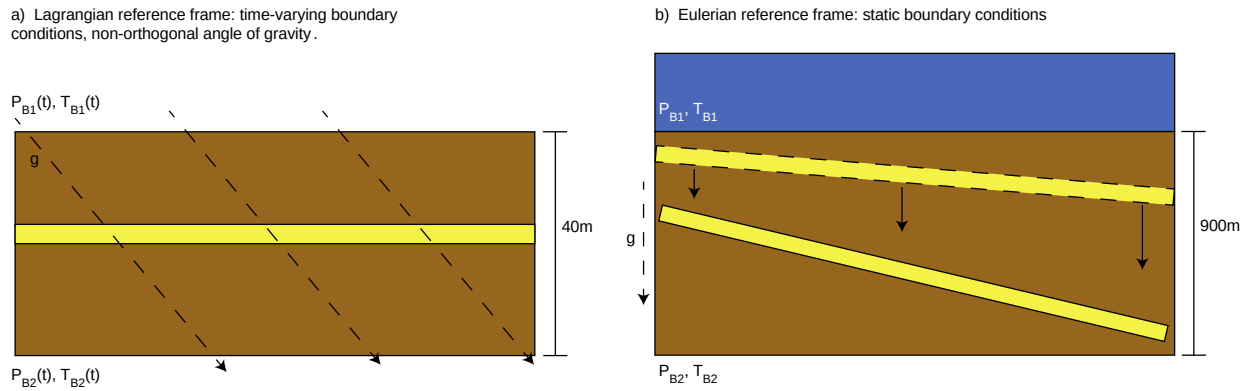

Figure 10. (a) A moving (Lagrangian) reference frame is used for 1-D and 2-D simulations of hydrate distributions within and around single sand layers. Dashed lines represent the gravity vector, which rotates to simulate the dip of the sand in 2-D. (b) A static (Eulerian) reference frame is implemented in this study for 3-D basin-scale simulations. Modified from Nole et al. (2017).

2.3.4 Incorporating heterogeneity from seismic data

In addition to simulating hydrate growth in simple reservoir geometries in the reference frames described above, this study developed algorithms for linking interpreted seismic data with the discretized simulation environment. In particular, this study used interpreted seismic data to inform the geometry of reservoir units and to add in seafloor topography. In 3-D simulations, reservoir horizons are first interpreted in seismic data; the base and top of each horizon are assigned Cartesian coordinates. The algorithm then maps these coordinates to the nearest grid block in the discrete simulation volume, whose resolution is typically significantly lower than that of the seismic data. The result of mapping from the reference coordinate system to the simulation domain for layered hydrate reservoirs in the Terrebonne Basin, Gulf of Mexico, is shown in Figure 11.

In addition to mapping reservoir geometries identified in seismic data to grid cells in the simulation domain, the simulator has also been designed to flexibly incorporate seafloor topography from imported seafloor depth information. While the finite volume scheme does not require rectilinear grids (it only requires grid blocks to be orthogonal), rectilinear systems were used predominantly in these simulations because of their ease of formulation and runtime efficiency. Therefore, seafloor topography was incorporated by applying a transform to discretized system imported from seismic data that considers a flat seafloor with varying water depth, expressed as spatially varying hydrostatic head along the simulation's top boundary (Fig. 12). This also transforms the geometry of the reservoir units. After the simulation is run, the system is transformed back into one with variable seafloor topography.

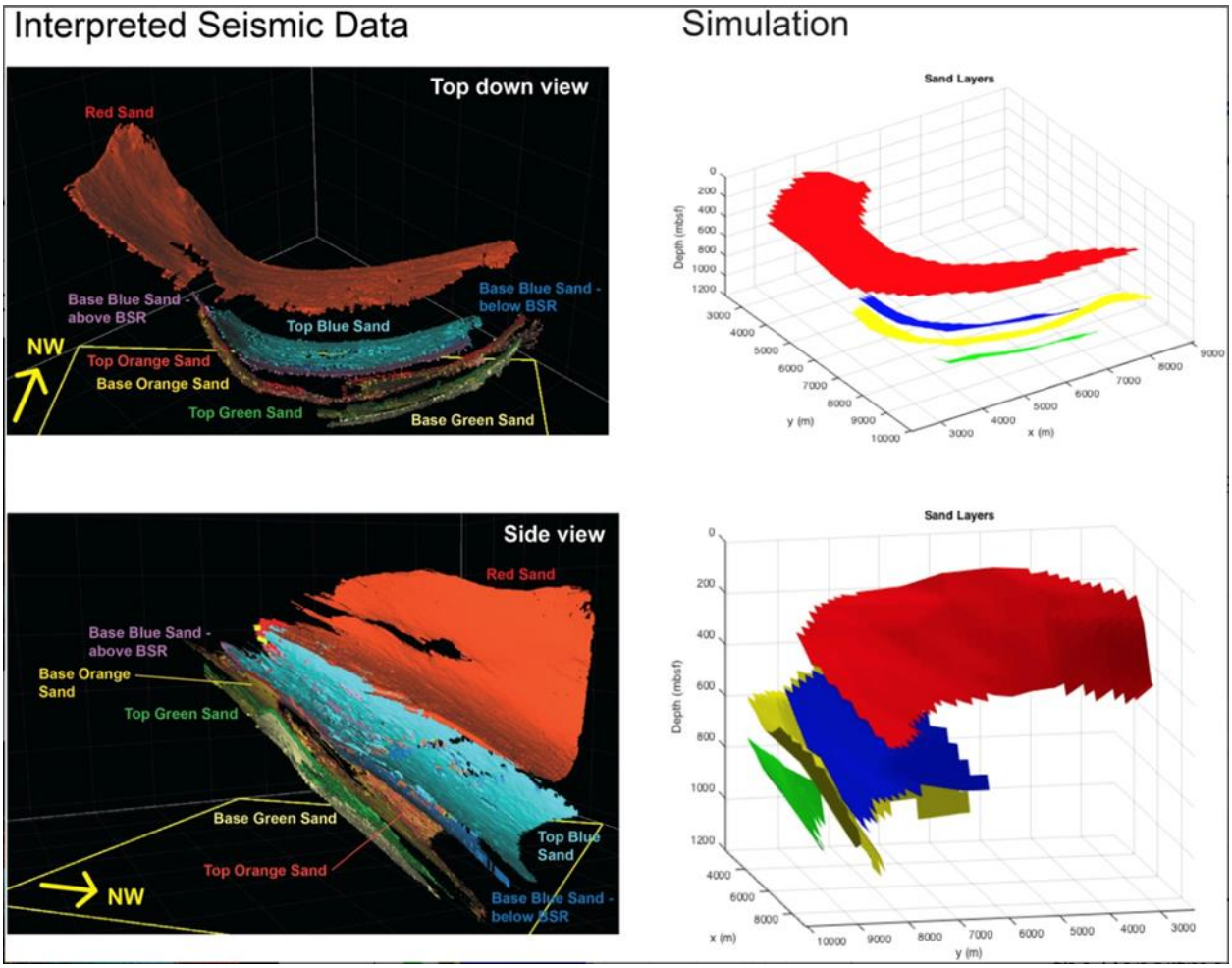

Figure 11. Three-dimensional perspective of interpreted sand horizons (left), which are imported into the simulator as horizons (right). Data for image used courtesy of WesternGeco. Modified from Nole et al. (2017).

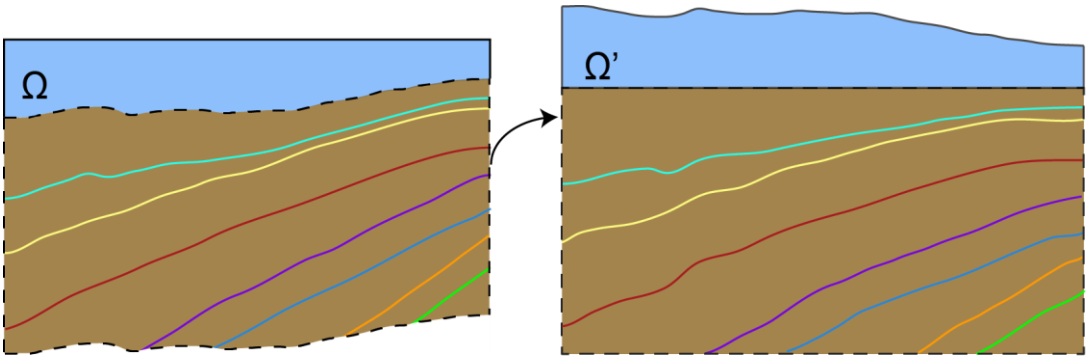

Figure 12. To include the effects of seafloor topography, seismic data is transformed from the irregular boundary Ω (outlined in a black, dashed line) into the rectangular grid system Ω'. Light blue region indicates hydrostatic head.

3. Hydrate formation from dissolved methane

3.1 Short migration

Short migration is the movement of microbially generated methane into coarser-grained layers by diffusion. We developed a model to investigate whether it could result in hydrate accumulations like those observed in the Terrebonne Basin. We initially modeled hydrate formation in a thin sand layer using a 1-D model assuming microbial methanogenesis in the surrounding clays with a constant value of α_{SMT} = 0.5 wt% and $\lambda = 10^{-13}$ s^{-1}. The sand was assumed to have a 100-fold difference in pore size from the clay (1 μm vs. 100 nm). In this case, when the sand reached a depth of about 300 mbsf, which is roughly the depth of the red sand in Hole H, hydrate had accumulated to a saturation of about 3.6%, and the distribution of hydrate exhibited slightly higher hydrate amounts at the upper and lower interfaces of the sand relative to the middle (Fig. 13), as predicted by modeling methane diffusion from the surrounding sediments (Rempel, 2011). Hydrate-free regions are visible above and below the sand, which is consistent with observations by Cook and Malinverno (2013) regarding the distribution of hydrate around the red sand in WR313 H.

Having shown that short migration can recreate the characteristics of hydrate distribution observed in the red sand, we next tested some more realistic scenarios. First, we reassessed the 1-D simulations assuming that the sand has a distribution of pore sizes rather than a single pore size. We assumed a lognormal distribution with a median pore radius of 20 μm and a pore radius standard deviation of 0.83 natural logarithm cycles based on analyses by Bihani (2016). Methane solubility was also updated to include the effect of restrictions on pore space caused by the formation of hydrate. With a 3.6 m thick sand, which is closer to the actual thickness of the red sand at Hole H, we found that maximum hydrate saturations of around 90% were possible (Fig. 14). This further suggests that the hydrate abundance and distribution in at least the red sand can be explained entirely by short migration of microbial methane. Note that hydrate saturation in the sand reaches a maximum around 600 mbsf and then decreases with further burial. This is due to the exponentially decreasing methanogenesis rate with depth combined with increasing solubility, resulting in a progressive dissolution of hydrate with burial.

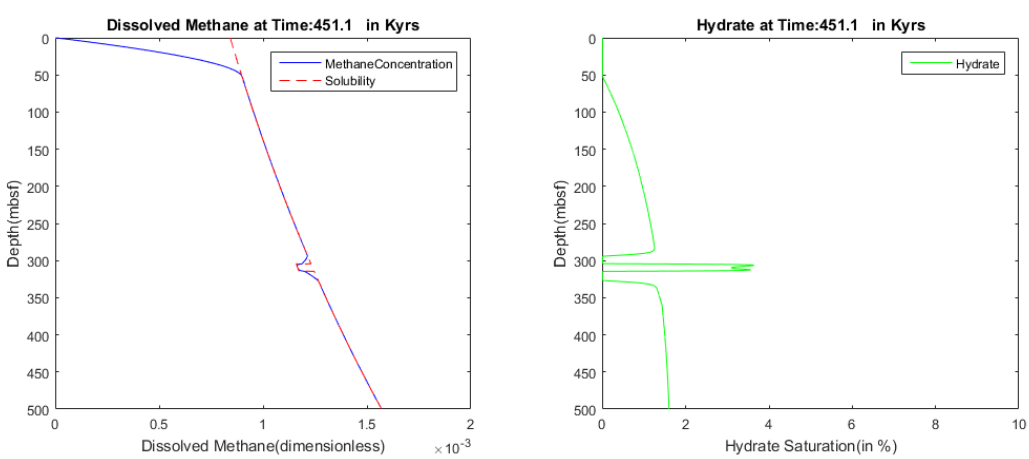

Figure 13. Methane concentration (left) and hydrate saturation (right) in a 1-D simulation of short migration of microbial methane into a thin (10 m thick) sand layer after 451.1 kyr of sedimentation.

We additionally tested the effect of sand thickness on hydrate distribution when methane is supplied by short migration alone. Since the hydrate distribution in the sand is characterized by maxima at the sand-clay interfaces and a minimum in the middle of the sand, we computed the ratio of minimum to maximum hydrate saturation in sands of different thickness following burial to 300 mbsf. As shown in Figure 15, sands thicker than about 10 m will have little to no hydrate in their centers, while a nearly uniform distribution will be attainable in sands thinner than about 2 m. Related to this is the fact that thicker sands will tend to have lower average hydrate saturations because less methane can penetrate to the center of the sand. In Figure 16, we have modeled sands of varying thickness buried to the depths of the red, orange, and blue sands in the WR313 H well. The trends of average hydrate saturation with the inverse of thickness are shown as solid lines. While the average saturation interpreted from downhole logs in the red sand in WR313 H is consistent with these thickness-dependent trends, only about 19% of the hydrate in the orange sand and about 10% of the hydrate in the blue sand can be attributed to short migration. However, these deeper sands contain interbedded sands and clays to a degree that is not necessarily reflected in the logs (Boswell et al., 2012), so it remains possible that short migration could have been more significant than we have accounted for.

We performed 2-D simulations to assess how dip of the sand layers might play a role in methane transport and hydrate accumulation. In these simulations we assumed that the sediments were horizontal at the time of deposition, and dip increased with burial. Parameters were the same as in the 1-D simulations, including the pore size distribution in the sand. We found that, at early time (Fig. 17a), the hydrate distribution was similar to that obtained in the 1-D simulations (cf. Fig. 13). However, as the sand is buried, hydrate in the bounding clays tends to dissociate and migrate into the sand, causing the sand to increase in hydrate saturation at the expense of hydrate in the clays (Fig. 17b). This effect eventually slows down as the gradient in methane concentration orthogonal to the sand layer relaxes, reducing the diffusive flux of dissolved methane (Fig. 17c). This 2-D example illustrates how the complexities of dissolved methane concentration gradients affects short migration over geologic time.

We finally performed 3-D simulations using sand geometries defined from seismic data. These simulations necessarily had a coarser resolution than the 1-D and 2-D simulations, resulting in a minimum sand thickness of 18.3 m. Due to this, the hydrate saturations in the sands were lower than those obtained in the 1-D and 2-D simulations. As in the 2-D simulations, sediments were assumed to be deposited horizontally and to have acquired dip during burial. The results after about 1 Myr are shown in Figure 18. Hydrate saturations generally increase downdip within the sands, which is consistent with the 1-D and 2-D results. A vertical profile taken in roughly the location of the WR313 holes illustrates a similar trend in hydrate saturation to Figure 14, with hydrate saturation reaching a maximum in the orange sand around 600 mbsf and then decreasing with further burial. Note also the decreasing amount of hydrate in the clay layers immediately beneath each sand as depth increases. This is due to similar phenomena as those shown in Figure 16. Overall, the 3-D simulations show that hydrate distribution in the Terrebonne Basin follows the trends that can be discerned at finer resolution in 1-D and 2-D models, and suggests that much of the hydrate that is present may have formed by short migration.

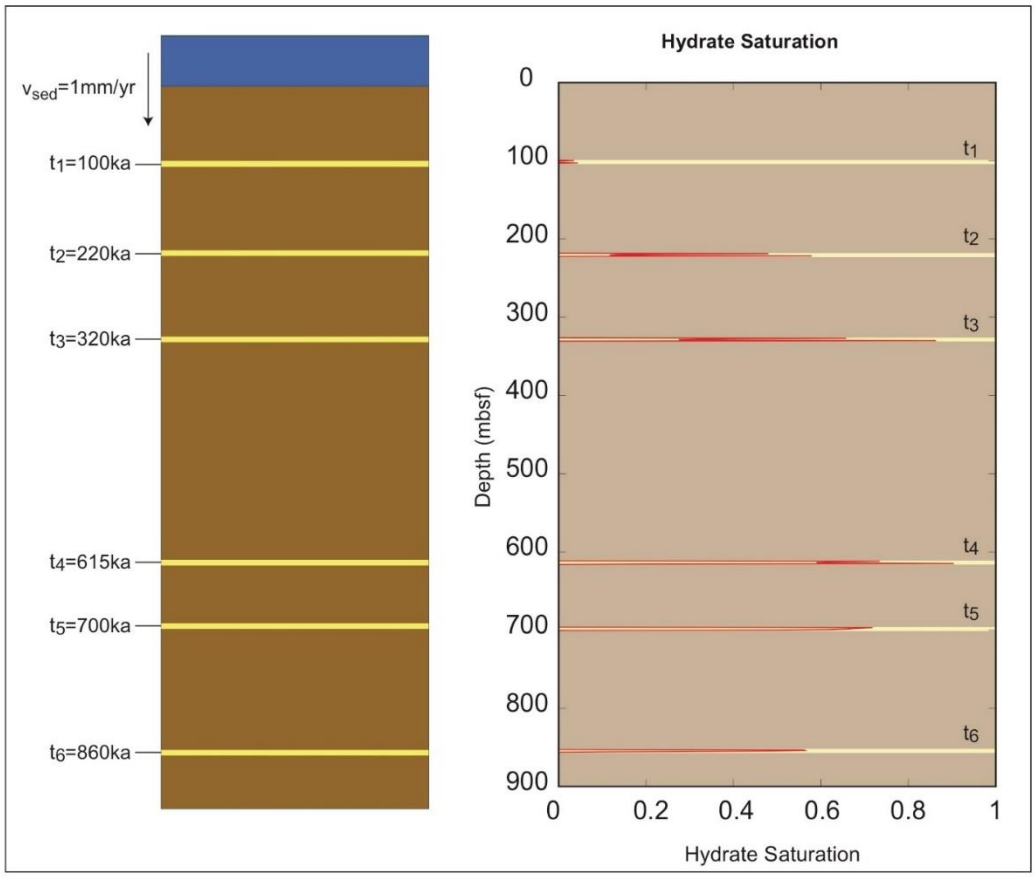

Figure 14. One-dimensional time-series evolution of hydrate saturation profiles within a single thin sand layer (3.6 m thick) as it is buried through the hydrate stability zone, incorporating capillary effects on diffusive aqueous methane concentration gradients. Modified from Nole et al. (2017).

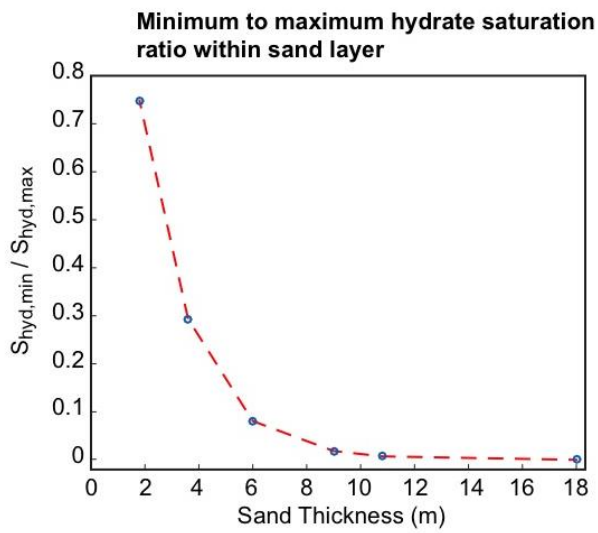

Figure 15. A comparison of minimum to maximum hydrate saturation within a sand for varying thicknesses of sand layers bounded by clays. Modifed from Nole et al. (2017).

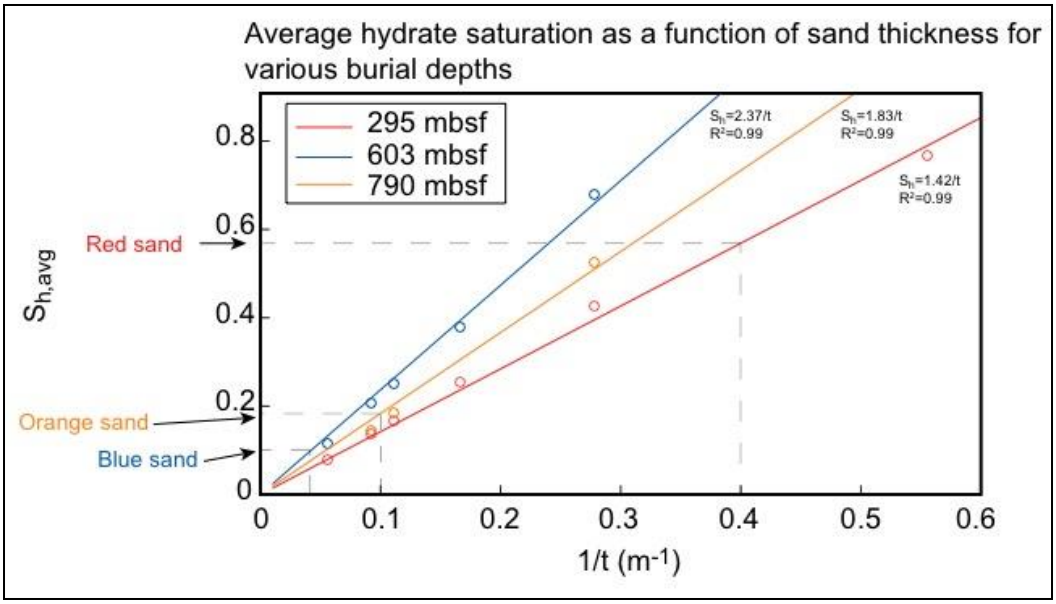

Figure 16. Average hydrate saturation as a function of sand thickness for various burial depths. Modified from Nole et al. (2017).

3.2 Advective transport

Because the sands penetrated in the WR313 holes appear to be continuous downdip through the base of the MHSZ on seismic data (Fig. 3), it is possible that methane is supplied to these sands by migration from some source below the MHSZ (Boswell et al., 2012; Frye et al., 2012). To investigate the feasibility of this migration mechanism in generating the observed hydrate occurrences, we performed 3-D simulations of hydrate accumulation due to advection of dissolved methane from below the base of the MHSZ. In these models, there was no microbial methanogenesis, and the methane was supplied at a flow rate dictated by compaction-driven flow (about 1 mm/yr). The dissolved methane concentration at the base of the MHSZ was assumed to be equal to the solubility value. As shown in Figure 19, the maximum hydrate saturation occurred at the base of the sand layer and was about 25%. It must be kept in mind that this simulation was subject to the same resolution constraints as the 3-D simulations of diffusive methane transport and that this hydrate saturation may be an underestimate. The methane flux entering the base of the MHSZ was roughly 9×10^{-11} kg/m^3/s, which is about 10 times the maximum flux achieved by microbial methanogenesis.

We additionally modeled hydrate accumulation through a hybrid migration mechanism we have termed “short advection.” In this scenario, methane is produced microbially in clays, but pervasive compaction-driven fluid flow moves the methane around and channels it into higher-permeability sands. In the case of horizontal sand layers, hydrate will only accumulate at the base of the sand (Fig. 20, top row), but in the case of dipping or vertical sands, as hydrate accumulates in the downdip portion of the sand, fluid flow will be deflected around the lower-permeability hydrate-bearing sands and supply methane farther updip in the sand (Fig. 20, middle and bottom rows). This may represent an attractive way of getting hydrate farther updip in sands as has been observed at WR 313. Our simulations of short advection have shown that higher hydrate

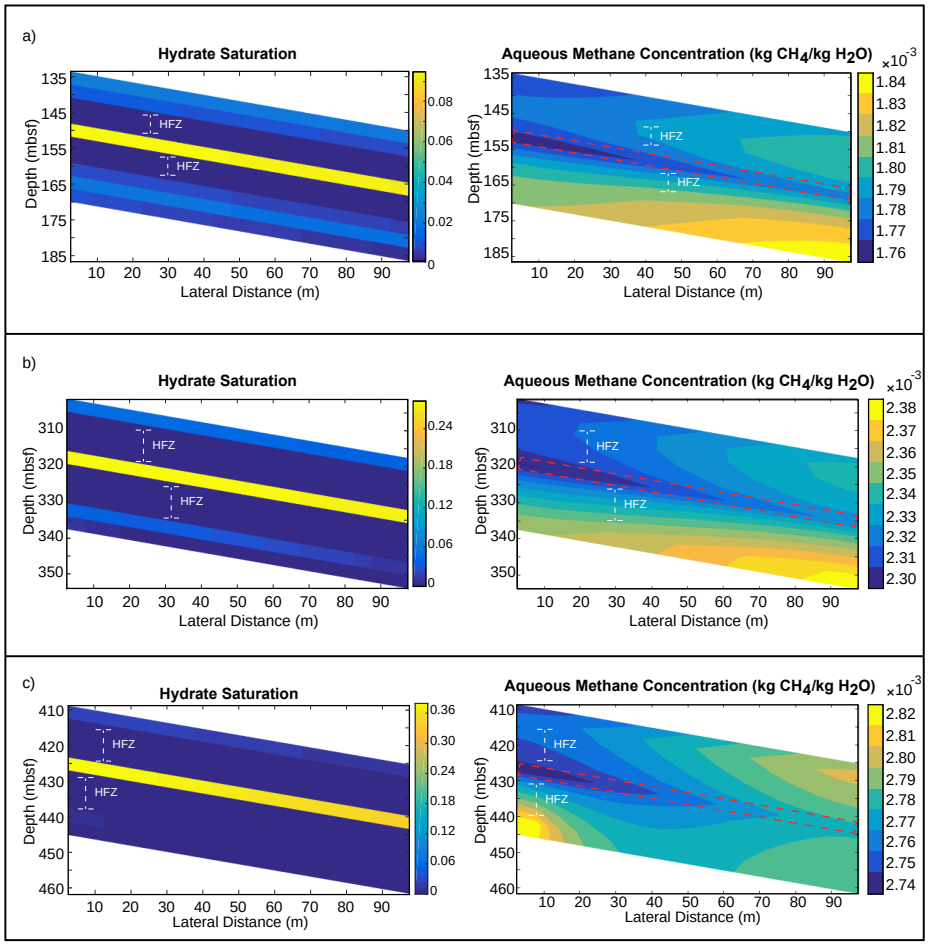

Figure 17. Simulated hydrate saturations, separated by hydrate free zones (HFZ), and dissolved methane concentrations in a dipping, 3.6 m-thick sand layer as it is buried through the hydrate stability zone at different stages of burial. Modified from Nole et al. (2017).

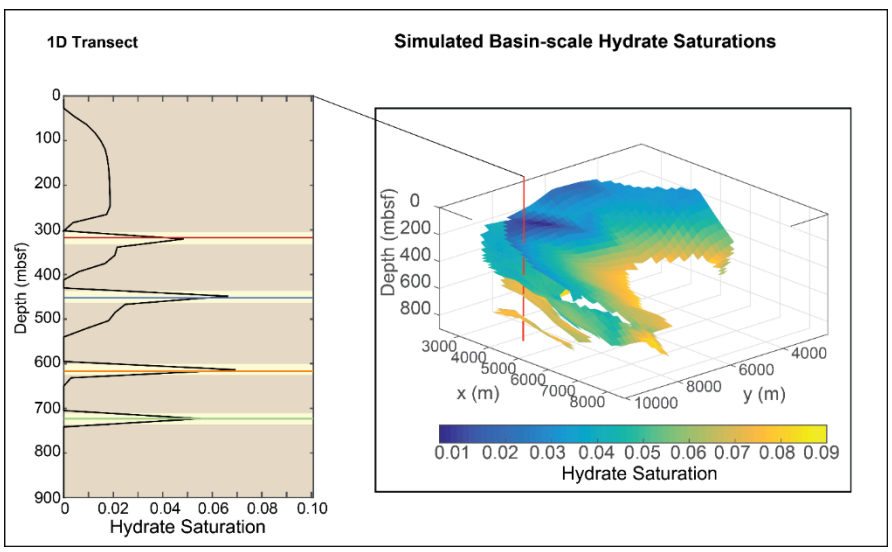

Figure 18. Three-dimensional simulated gas hydrate saturations in 4 sand layers (18.3 m-thick), accompanied by a 1-D transect after ~1 million years. In the 1-D transect, sand layers are highlighted in yellow, and clays are highlighted in brown. Modified from Nole et al. (2017).

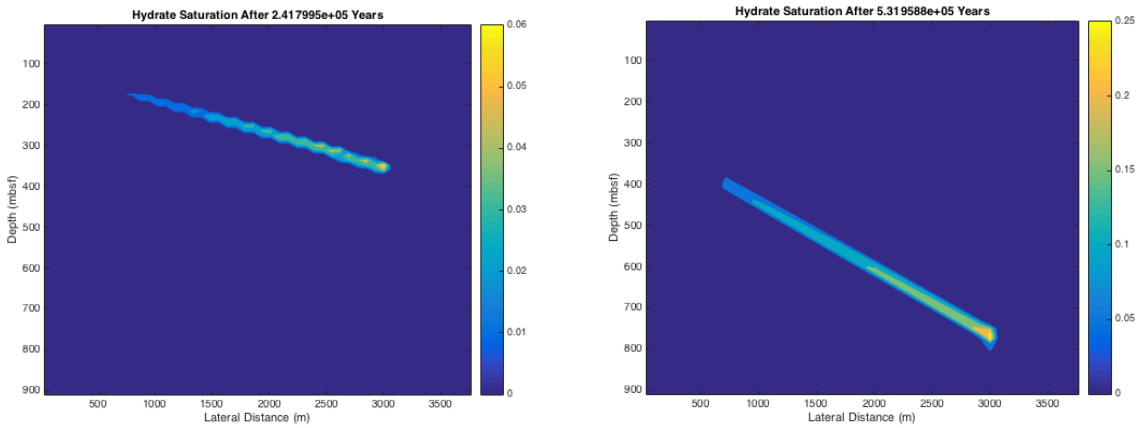

Figure 19. Hydrate saturation in an advective system. Colors show hydrate saturation in a dipping sand layer. Left: intermediate time. Right: final time (when base of sand reaches base of MHSZ).

saturations may be achieved than with diffusion or advection alone (Fig. 21). For instance, our simulations predict a maximum hydrate saturation of 35% in a dipping sand.

3.3 Remarks on dissolved methane

Having performed simulations of both diffusion and advection, we compared the methane fluxes in each case to other estimates of methane flux in the northern Gulf of Mexico and other sites worldwide. Table 1 shows a comparison of our results with other estimates of methane flux due to microbial methanogenesis. Our results are about an order of magnitude higher than other estimates, which suggests that the fluxes necessary to produce the observed hydrate deposits cannot be maintained for long periods of geologic time. Transient organic matter deposition at the seafloor (Malinverno et al., 2018) may be a more likely scenario.

Table 2 shows comparisons of our work with other estimates of advective methane supply. The methane flux we calculate for advection of dissolved methane is lower than some other sites worldwide but is similar in magnitude to an estimate from Keathley Canyon, which is also located in the northern Gulf of Mexico. We interpret this as evidence that advection cannot be ignored as a significant methane migration mechanism.

If short migration and/or short advection are dominant modes of methane supply to the sands in the Terrebonne Basin, high hydrate saturations in sands deeply buried in the MHSZ are anomalous because our simulation results suggest that hydrate will dissolve at depth as solubility increases and the microbial methane supply dwindles. This situation could be mitigated by some means of preserving hydrate in the clay layers between sands. One such possibility is the formation of fracture-hosted hydrates in the clays (Cook et al., 2014). These hydrates would act as repositories of microbial methane, which can supply methane to the sand layers at depths where microbial methane supply is negligible. Hillman et al. (2017) show that several clay units with fracture-hosted hydrates may be present at WR313 as interpreted from seismic data (Fig. 22). This may provide evidence of such a microbial methane repository.

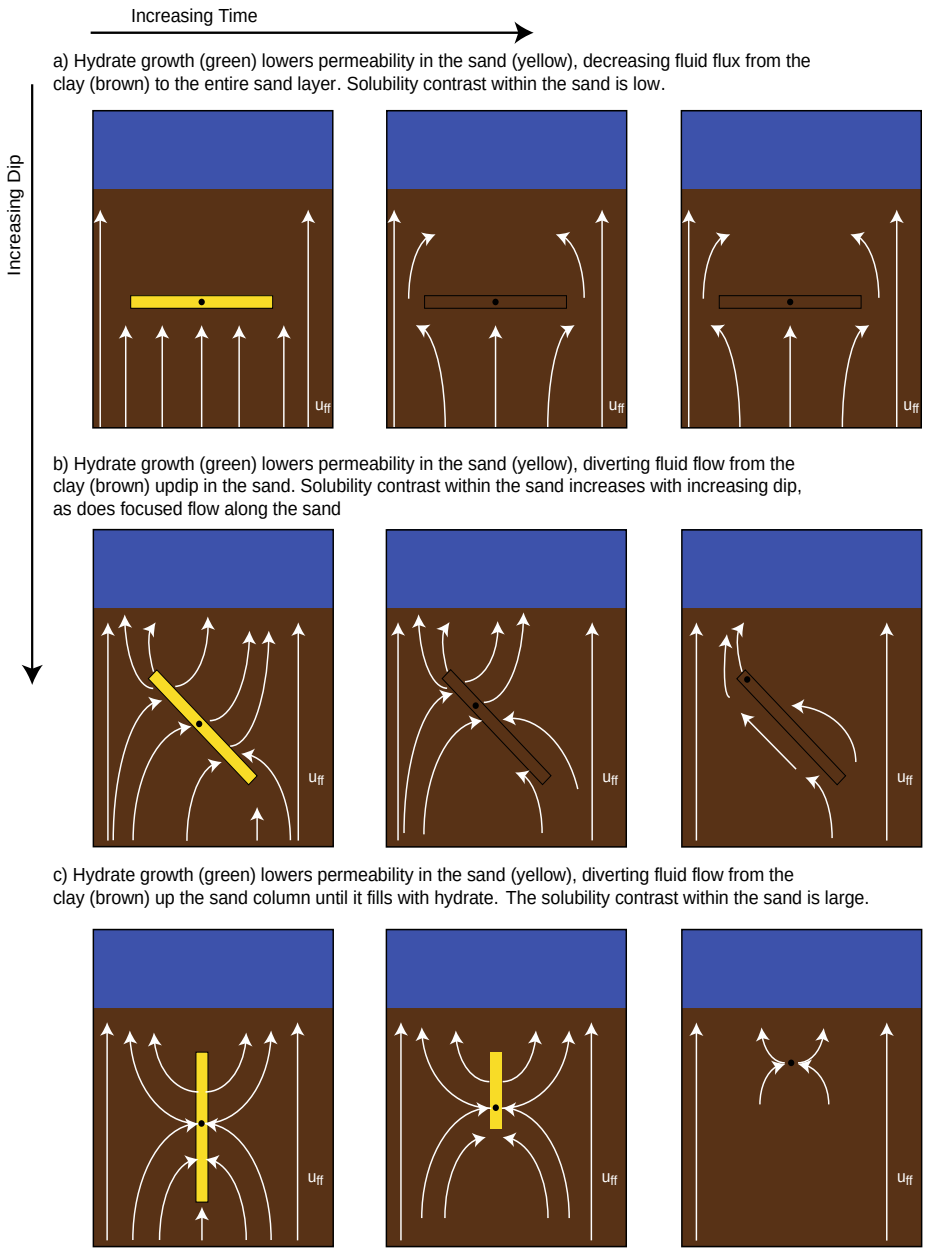

Figure 20. Hydrate accumulation in sand layers with different orientations by short advection. White arrows represent fluid flow; green shading represents hydrate accumulation. Modified from Nole et al. (2016).

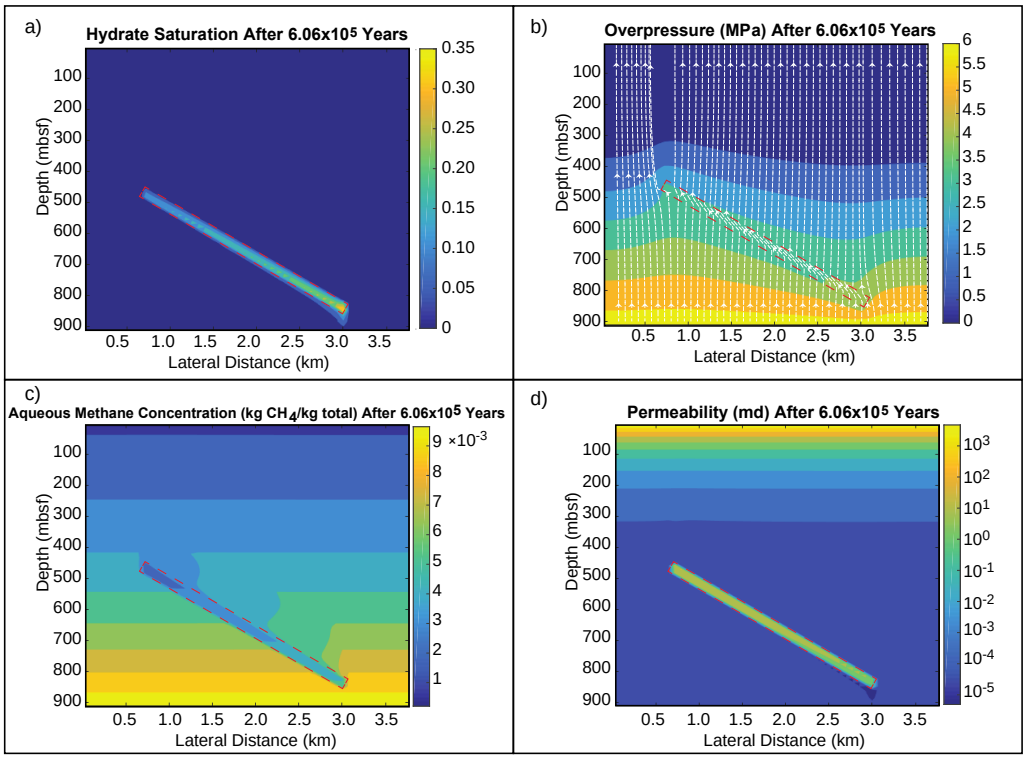

Figure 21. Simulation results for short advection of methane into a dipping sand. (a) Hydrate saturation. (b) Overpressure and fluid flow streamlines. (c) Aqueous methane concentration. (d) Permeability.

Methanogenesis rate ($kg/m^3/s^1$)	Location	Reference
10^{-12}, 10^{-11}	Walker Ridge, N GOM slope	This study
4×10^{-14}	Green Canyon, N GOM slope	Frye (2008)
5×10^{-13}	IODP Site U1325, N Cascadia margin	Malinverno (2010)
3×10^{-13}	IODP Site C0002, Nankai Trough	Malinverno and Goldberg (2015)
6×10^{-14}	NGHP-01 Site 17, Andaman basin	Malinverno and Goldberg (2015)

Table 1. Comparison of methane fluxes from microbial methanogenesis. Lower rate for Walker Ridge was used in 1-D and 2-D simulations; higher rate was used in 3-D simulations.

Advection rate ($kg/m^3/s^1$)	Location	Reference
9×10^{-11}	Walker Ridge, N GOM slope	This study
1×10^{-11}	Keathley Canyon, N GOM slope	Daigle and Dugan (2010)
4×10^{-10}	NGHP-01 Site 10, K-G basin	Daigle and Dugan (2010)
3×10^{-9}	Hydrate Ridge	Daigle and Dugan (2010)

Table 2. Comparison of methane fluxes from updip advective migration of dissolved methane.

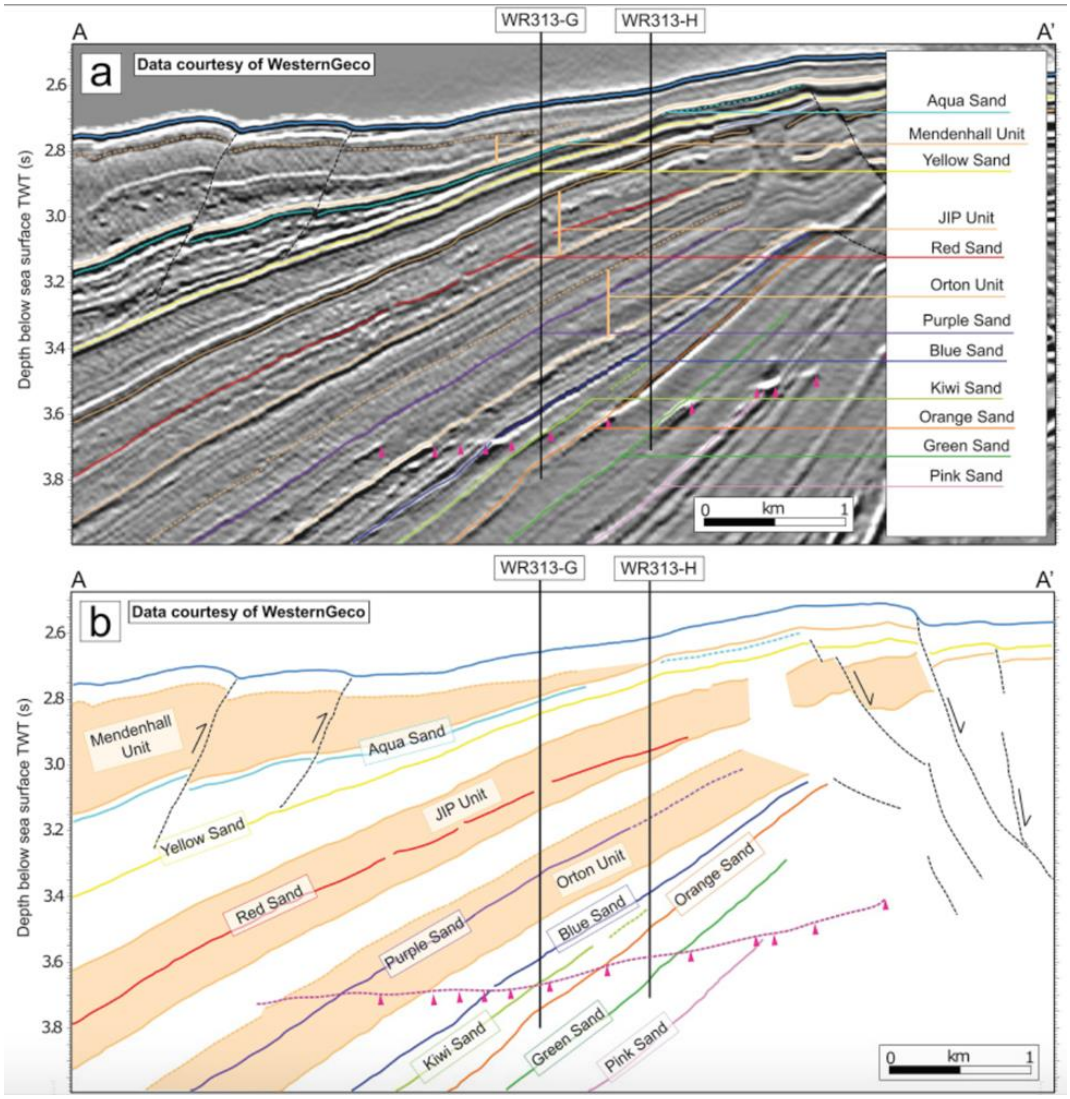

Figure 22. (a) Seismic profile extracted from the 3-D volume acquired in the Terrebonne Basin. (b) Interpretation of the seismic profile, showing the location of the key units (the Red, Blue, Orange, and Green sands) as well as additional water saturated sands and possible marine mud source units (tan colored). The position of the BSR is indicated by the pink arrows and dashed line. Figure from Hillman et al. (2017).

We investigated the effect of time-dependent organic carbon deposition on the formation of isolated hydrate-bearing intervals in fine-grained sediments (Malinverno et al., 2018). The hypothesis was that enhanced deposition of labile organic carbon on the continental slope during Pleistocene glacial periods of low sea level led to enhanced microbial methanogenesis in the corresponding sediment interval. We modeled gas hydrate formation with a time-dependent organic carbon deposition at the top driven by glacioeustatic cycles, and found that the model predicted hydrates should be present at depths 200-400 mbsf. The model predictions match hydrate-bearing intervals observed in LWD sites drilled in the Terrebonne basin (WR313-G and WR313-H) and Green Canyon Block 955 (GC955-H). The resulting hydrate-bearing intervals may provide a source of dissolved methane once these hydrates are buried deeper and dissolve due to the increasing methane solubility.

4. The role of a discrete gas phase

4.1 Introduction

This section focuses on understanding the phase behavior when hydrate-bearing sediments are buried beneath the BHSZ. To begin, we consider a gas hydrate system at bulk equilibrium with its surrounding pore water (Fig. 23a). Hydrate (green circles) beneath the seafloor occupies a fraction of the pore space of a reservoir unit (yellow), with the rest of the pore space containing the aqueous phase (blue circles). As soon as this system is buried past the bulk BHSZ, all methane present as hydrate is converted into gas. Because of differences in methane mass fraction and volume between hydrate and gas, and because hydrate dissociation releases water in addition to methane, the volume of pore space occupied by hydrate is not entirely replaced by gas. But the occurrence of hydrate above the BHSZ is completely separated from the occurrence of gas below it, and both phases cannot coexist at any depth other than the depth of the BHSZ.

When a hydrate reservoir unit contains a distribution of pore sizes, this picture becomes more complicated (Fig. 23b). Instead of hydrate being the only stable phase above a single depth and gas being stable below this depth, hydrate as a nonwetting phase occupies the largest pores but also a set of successively smaller ones, with water always occupying the smallest pores and coating pores of all sizes. Hydrate in small pores is actually stable at depths below the bulk BHSZ (Liu and Flemings, 2011) resulting from the Gibbs-Thomson Effect.

When sediments containing gas hydrate are buried through the MHSZ, methane solubility continuously increases with burial depth because the rate at which temperature increases along the geotherm (destabilizing hydrate) exerts greater control over hydrate phase stability than the corresponding increase in hydrostatic pressure (stabilizing hydrate). Therefore, considering an isolated system in the absence of any external methane sources, the burial of a hydrate mass results in thermodynamic disequilibrium: hydrate is present in pore space, but the concentration of methane in pore fluid is below solubility, meaning hydrate is unfavorable in the smallest pore. To re-equilibrate, methane is added to the pore fluid via hydrate dissolution, which increases aqueous methane concentrations at the expense of hydrate saturation. If hydrate is not present in sufficient quantities to supply the required amount of methane, all of the hydrate will be driven to dissolve. This process was described in §2.2.2.

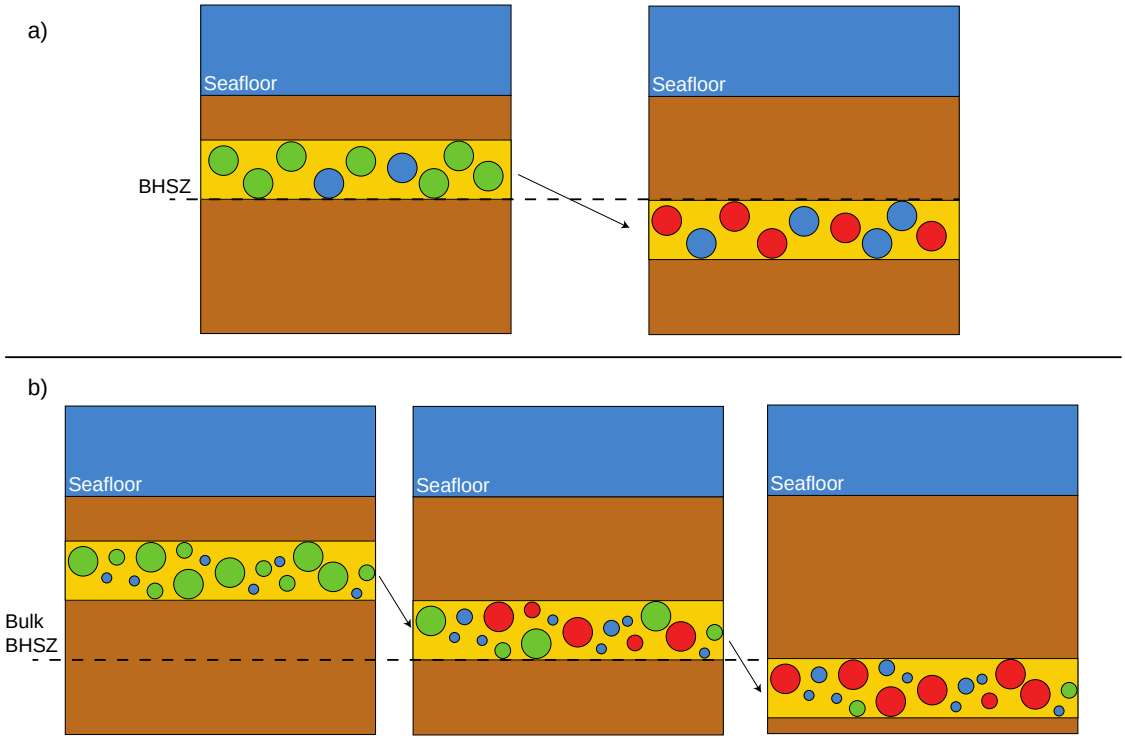

Figure 23. (a) Bulk dissociation of gas hydrate upon burial beneath the base of the hydrate stability zone (BHSZ), and (b) dissociation of gas hydrate in pores characterized by a pore size distribution.

4.2 Modeling methane recycling

For these simulations, we keep the salt mass fraction constant throughout the simulation at 35 kg/m^3 (seawater) to isolate the effects of pore size distributions on methane recycling. Salt exclusion during hydrate formation enhances local salinity and therefore locally inhibits hydrate formation, so gas could potentially be propelled further upward into the hydrate stability zone relative to the simulations presented here, but over geologic time diffusion and gravity flow would likely dampen the salinity effect. In diffusion-dominated systems within the gas hydrate stability zone, salt motion has been shown to be negligible (Nole et al., 2017; You and Flemings, 2018), but incorporating salt motion is the subject of future work.

Simulations in this study adopt a Lagrangian reference frame, where domain boundary conditions are formulated as functions of time and reflect continuous burial through the gas hydrate stability zone. Each simulation is initialized with a particular saturation of gas hydrate (fraction of pore space) contained in reservoir pores. Everywhere, dissolved methane concentrations are initially set to the solubility of methane corresponding to the effective pore radius governing hydrate growth. Temperature throughout the domain increases during burial along the geothermal gradient, and pressure increases along the hydrostatic gradient. Compaction during burial reduces porosity and drives a very small fluid compaction flux upward through the domain. Details regarding this formulation can be found in Nole et al. (2017).

As the domain is buried to the bulk base of the hydrate stability zone and then proceeds down to further depths, hydrate becomes less stable, and pores containing hydrate must eventually

transition to being gas-filled. The transition zone from hydrate to gas should depend on the initial saturation of hydrate present when the system reaches the base of the hydrate stability zone, because higher hydrate saturations are accompanied by higher aqueous methane solubility. Additionally, more methane stored in the hydrate phase should generate more gas upon full dissociation.

Model parameters were selected to emulate the gas hydrate system at Walker Ridge in the Gulf of Mexico. A deep seafloor (set to 2 km) and moderate geothermal gradient (18.5°C/km in these simulations) contribute to a relatively thick gas hydrate stability zone: in these simulations, the bulk base of the hydrate stability zone occurs at approximately 907 mbsf. Lognormal pore size distributions fit to nuclear magnetic resonance (NMR) laboratory measurements on samples from nearby Keathley Canyon indicate that clays in this region exhibit a median pore size of approximately 75 nm. Contrastingly, NMR data suggests that coarser units here exhibit median pore sizes of 10 microns (Bihani, 2016). For these simulations, we employ synthetic pore size distributions that span the range of lithologic heterogeneity encountered here as an approximation for average behavior in interbedded reservoir units at Walker Ridge. Pore size distributions used for these simulations are lognormal with a median pore size of 2 microns. In our synthetic pore size distributions, about 12% of the distribution (at nonwetting phase saturations above 88%) can be attributed to the measured clay lithology, and 8% (nonwetting phase saturations below 8%) constitute the sandy silt lithology from NMR data. Therefore, 80% of the synthetic pores used here are of sizes between the endpoints of our laboratory data. In the following discussion, we define the initial hydrate saturation as the saturation at which the simulation is initialized within the gas hydrate stability zone. Since methane solubility to the hydrate phase increases with increasing burial depth, hydrate must dissolve with burial to add methane to the aqueous phase. Therefore, hydrate existing above the BHSZ tends to dissolve over simulation runtime, which slightly decreases the saturation of hydrate in the pore space relative to the described initial hydrate saturation. The effect is only noticeably pronounced at very low saturations, which in fact can be useful in replicating bulk 3-phase equilibrium.

Simulation results indicate four 1-D profiles that, given varying initial hydrate saturations, appear to characterize the hydrate dissociation process. We argue only 2 of these profiles demonstrate true methane recycling (Fig. 24). First is a situation in which hydrate exists in such small quantities that, eventually, not enough methane is available to generate a free gas phase after hydrate dissolution. Second, when hydrate exists in quantities sufficient to generate a small amount of free gas but not enough to percolate through the medium, hydrate is entirely replaced by gas during burial. If enough hydrate exists initially, gas formed from hydrate can exceed the critical gas saturation of the medium and flow upward via buoyancy, recycling back into hydrate. Finally, at very high initial hydrate saturations, the system can experience multiple recycling fronts.

The simulation depicted in Figure 24a demonstrates two important features of bulk hydrate dissociation: all methane stored as hydrate is immediately converted to gas upon burial beneath the BHSZ, and below some particular (nonzero) hydrate saturation buried to the BHSZ a free gas phase cannot form. In Figure 24a, hydrate saturations are initialized at 2% of the pore space. Dissolved methane and methane hydrate can be considered to essentially be at bulk equilibrium because the pore size governing 3-phase equilibrium is relatively large (26 microns at 2%

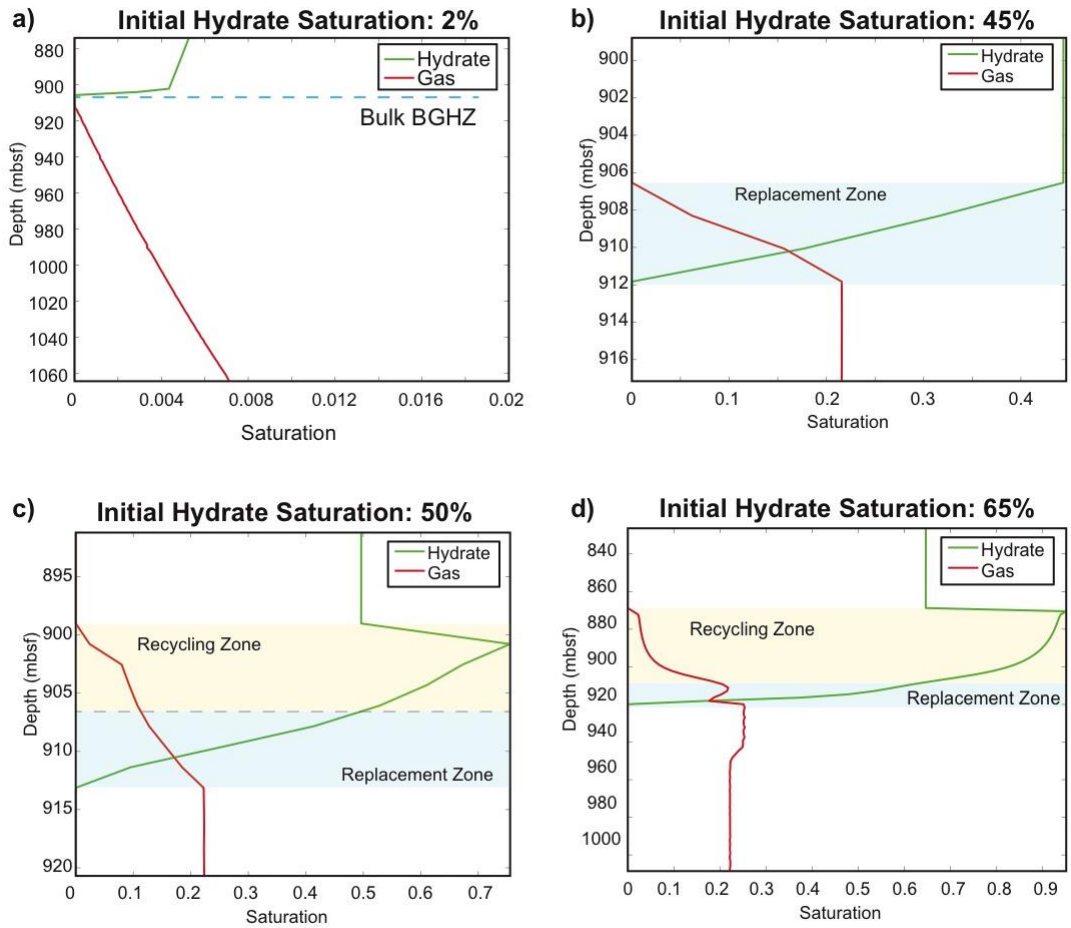

Figure 24. Simulated hydrate and gas profiles after burying sediments containing various initial hydrate saturations past the bulk BHSZ. Simulations are initialized with hydrate saturations of a) 2%, b) 45%, c) 50%, and d) 65%. Hydrate saturations at depths shallower than the BHSZ are slightly lower than the initial hydrate saturations because hydrate dissolves during burial due to an increase in solubility.

hydrate saturation). As this system is buried, hydrate dissolves into the aqueous phase due to increasing solubility of methane to the hydrate phase, which is why the hydrate saturation at the top of Figure 24a is only about 0.5%; saturation increases as depth decreases, and at some distance about the bulk BHSZ it reaches the initial value of 2%. Once the system approaches the base of the hydrate stability zone (about 907 mbsf in these simulations), the pressure and temperature of the system pass 3-phase equilibrium. With further burial beneath the hydrate stability zone, three-phase equilibrium pressure remains higher than the pore pressure, so all remaining hydrate is directly converted into free gas. As hydrate saturation above the base of the hydrate stability zone decreases with further burial, less methane is available to grow gas beneath the base of the hydrate stability zone. The gas phase saturation therefore decreases at the BHSZ over time, leading to the gas profile illustrated in Figure 24a, where gas saturation diminishes with decreasing depth. Note that this simulation was run for a sufficient length of time to build an appreciable gas column beneath the BHSZ. Thus, there eventually arrives a point at which hydrate does not exist in sufficient quantities in sediment pore space to even grow a free gas phase: in the simulations presented below, this occurs approximately below 0.2% hydrate saturation (Fig. 24a).

When moderate amounts of gas hydrate are present above the base of hydrate stability, hydrate dissolving through burial releases enough methane to generate a free gas column beneath the MHSZ that is separated from the MHSZ by a region of transition from hydrate to gas, referred to here as the replacement zone (Fig. 24b). A distribution of pore sizes necessitates this region; the thickness of this zone depends on the pore size magnitude and breadth of the pore size distribution (see Liu and Flemings, 2011). The total amount of free gas in saturation units that is generated through hydrate dissociation is approximately half of what was initially present as hydrate at the given pressure and temperature conditions of this simulated environment. Although the gas phase is less dense than the hydrate phase, the mass fraction of methane in the gaseous phase is almost 100%, while the mass fraction of methane in the hydrate phase is 12.52%. For an average gas density of 220 kg/m^3 at these pressure and temperature conditions, 10% gas saturation would correspond to 22 kg of CH_4/m^3 of pore space; in a methane hydrate mass with a density of 900 kg/m^3, an equivalent amount of methane would correspond to 19.5%, or nearly twice as much, hydrate.

In this scenario (Fig. 24b), enough methane can be supplied to consistently produce a free gas phase; furthermore, a thin replacement zone exists in which methane stored in hydrate transitions to methane stored in gas. Free gas, hydrate, and an aqueous phase can all coexist in 3-phase equilibrium in this zone because methane transitions from existing in small pores hydrate at the top of the transition zone in the absence of gas, to hydrate and gas in separate pores, to all gas for a three-phase zone thickness of about 7 m. Note that, in Figures 24b-c, the hydrate saturation is constant above the shallowest gas occurrence, in contrast with Figure 24a. This is because the mobile gas can replenish the hydrate that is lost due to solubility increase.

In order for recycling to occur, enough of a free gas phase must be generated through hydrate dissociation such that the upward gas buoyancy flux outpaces burial consistently throughout the replacement zone. Otherwise, gas will be buried before it can add any methane above the replacement zone. In the simulations presented here, the threshold at which methane can actually be recycled is crossed at about 50% hydrate saturation (Fig. 24c). When methane recycling occurs, a distinct region forms above the replacement zone in which hydrate saturations increase steadily to a peak before then dropping off sharply back to the incoming hydrate saturation. This steady blockage of pore space with hydrate and intrusion of gas can be better understood by examining the evolution of aqueous methane concentrations as the system is buried.

In Figure 25a, hydrate is initially present in pores (~1 micron) whose aqueous methane solubility is close to bulk solubility (green line at t_1). At this point, a free gas phase is present in the large pores but is not interconnected, and hydrate still occupies the small pores. At t_2 (blue line), enough gas is buried beneath the hydrate stability zone that a significant mobile gas column can form. Now, gas moving up from depth encounters pore space already containing gas, so dissolved methane concentrations increase as gas moves upward. Once gas reaches a depth at which hydrate is stable in large pores, dissolved methane added to the system partitions the large pore space between hydrate and gas. Hydrate becomes more stable as gas migrates upward, so a greater proportion of gas is converted into hydrate, which decreases gas saturation and reduces the relative permeability of the medium to gas. This effect leads gas saturation to diminish as it moves upward while hydrate saturation increases into smaller pores. Methane concentrations

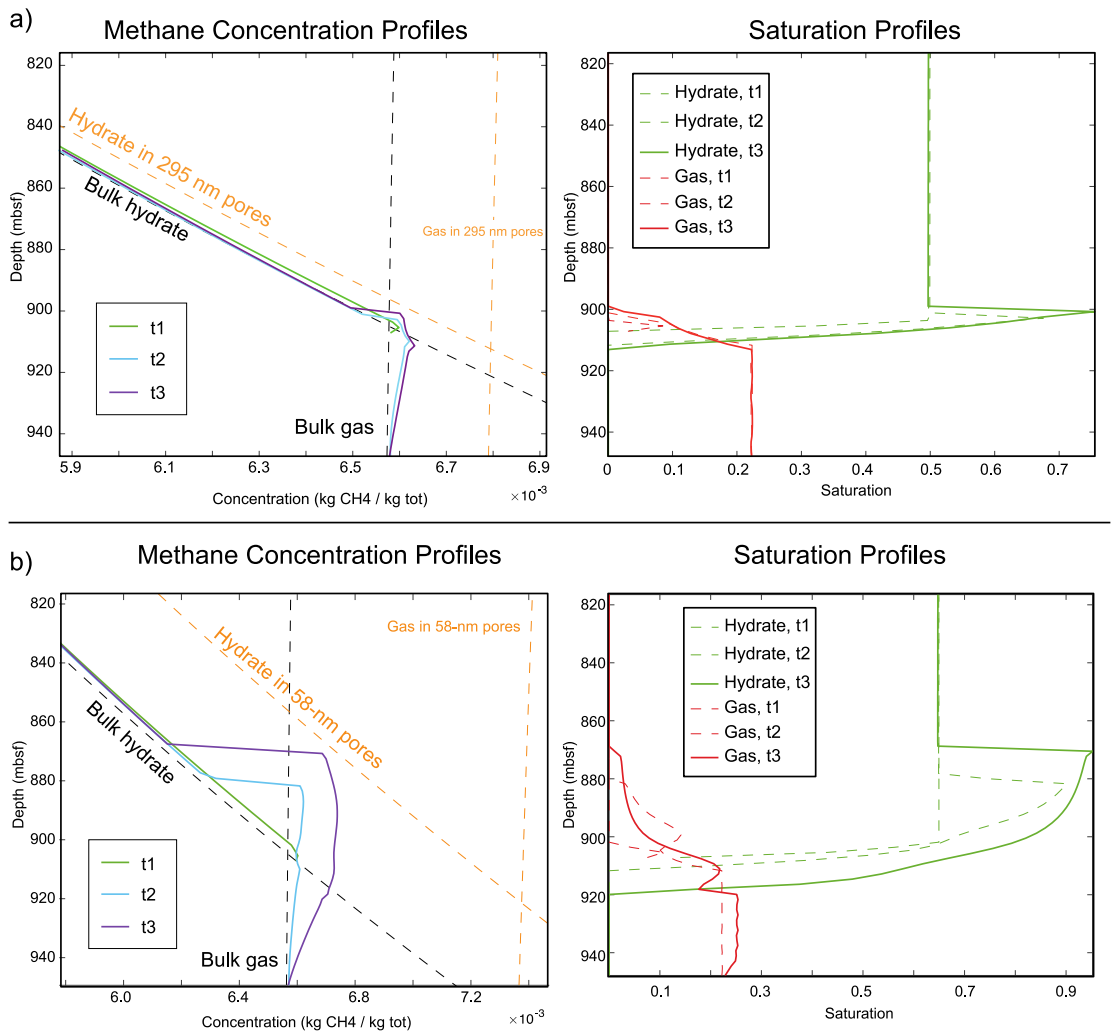

Figure 25. Methane concentration profiles and corresponding hydrate saturations at 3 distinct times during burial for initial hydrate saturations of a) 50% and b) 65%.

decrease upward past the BHSZ, but they remain relatively constant within the 3-phase zone where hydrate and gas continuously reconfigure. By t_3 in Figure 25a, enough gas has been injected to shift the top of free gas occurrence by about 5 m (purple line). The 3-phase region in this particular example is fairly small, owing to the relatively low initial hydrate saturation.

At higher initial hydrate saturations (65% in Fig. 25d), massive amounts of methane from dissociated hydrate can be injected past the top of the replacement zone and into the recycling zone. In fact, so much methane is buried in this instance that gas saturations can increase moving upward through the replacement zone instead of monotonically decreasing. The analog is never true for hydrate saturation, however. This phenomenon occurs where there is a significant change in slope of the hydrate saturation profile, because sediments more highly saturated in hydrate release more methane upon dissociation. Thus, burial produces greater amounts of free gas from areas of higher hydrate saturation, and when there is a significant change in hydrate saturation throughout the 3-phase zone this can result in significant differences in gas mobility,

thus prompting gas accumulation where gas mobility changes abruptly. Additionally, over time the free gas region immediately below the hydrate stability zone will accumulate more and more free gas, which enhances gas mobility and methane concentrations in this region relative to earlier in burial when less hydrate was available for dissociation (Fig. 25b).

4.3 Methane flux necessary to form a gas phase

To assess the methane flux required to generate a discrete gas phase, we compared microbial methanogenesis rates and rates of compaction-driven flow. Our interpreted microbial methanogenesis rates at WR313 are 10^{-11} kg/m^3/s at maximum (Table 1). The minimum amount of methane required to form a gas phase anywhere in the MHSZ is equal to the solubility value right at the base of the MHSZ, which is 0.0027 kg/kg. If methane is generated at a constant rate in a control volume of sediment from the time of deposition to the time it is buried to the base of the MHSZ, which in this case is roughly 900 kyr, then 284 kg/m^3 of methane would be generated. Obviously, this is an overestimate since it depends on the availability of labile organic matter and assumes that methane is not converted to hydrate. In a more realistic scenario, our simulations have shown that microbial methanogenesis does produce enough methane to form hydrate and achieve solubility at the base of the MHSZ, and therefore a gas phase may be expected at WR313.

If a discrete gas phase were supplied from below the base of the MHSZ, again the methane concentration would need to exceed 0.0027 kg/kg or 2.8 kg/m^3. The interstitial velocity of fluid from compaction-driven flow in sands at the base of the MHSZ is estimated to be 2×10^{-6} m/s, so the total methane flux in sands at the base of the MHSZ would need to be at least 6×10^{-6} kg/s/m^2.

5. Conclusions

We studied the methane migration mechanisms and associated methane hydrate accumulation rates in coarse-grained sands of the Terrebonne Basin, located in Walker Ridge Block 313 in the northern Gulf of Mexico. Using a combination of one-, two-, and three-dimensional basin modeling, we have focused on two different methane migration mechanisms to form high-saturation hydrate-bearing sand layers: diffusive flux and advective transport of dissolved methane. In the case of diffusive flux, methane is generated microbially in finer-grained sediments and diffuses over short distances into adjacent sand layers where capillary effects favor precipitation of hydrate. In the case of advective transport, methane may be supplied either by long-distance flow along permeable layers into the MHSZ, or by short-distance advection of microbial methane that is focused into more permeable layers by compaction-driven flow.

We have found that these different migration mechanisms have distinct timescales and hydrate accumulation patterns. For example, diffusion into coarse-grained layers tends to form heterogeneous hydrate deposits, with hydrate concentrated on the upper and lower edges of the coarse-grained layers with little to no hydrate in the middle of the layers. Maximum hydrate saturations in these cases can be 30-40% of the pore space after ~1 Myr. At the basin scale, individual sand layers compete for methane produced in intervening clay layers. Because microbial methane is mostly generated at shallow depths, hydrate may only be preserved from

dissolution in sands during burial through the MHSZ if fracture- or vein-hosted hydrates form in adjacent clays, providing an additional supply of methane during burial. These fracture-hosted hydrates may form in response to transient deposition of organic-rich sediment at the seafloor, resulting in episodes of intense microbial methanogenesis.

If sediment compaction generates overpressure, compaction-driven flow can serve as an additional mechanism of focusing microbial methane into coarse-grained layers that act as conduits for fluid flow. Under these conditions, hydrate may fill 30-40% of the pore space after ~1 Myr, with hydrate distributed more homogeneously within sand layers, including far updip within the MHSZ. These saturations may be further enhanced by interbedding of sands and thin clay layers in which further microbial methanogenesis occurs.

Finally, we found that recycling of methane as the BHSZ can provide a significant source of methane to form hydrate above the BHSZ, and that pore size effects allow gas to coexist with hydrate for tens of m above the BHSZ, even in sandy sediments. This may be a mechanism of delivering recycled methane to much shallower depths within the MHSZ, and could reduce the amount of microbial methane that is necessary to form massive hydrate deposits.

Our work has demonstrated the importance of microbial methanogenesis, short-distance migration, pore water advection, and lithologic heterogeneity on generating the massive hydrate deposits in the Terrebonne Basin.

References

Amyx, J.W., Bass, D.M., Whiting, R.L., 1960. *Petroleum reservoir engineering: Physical properties*. McGraw-Hill, New York, N.Y.

Anderson, R., Tohidi, B., Webber, J.B.W., 2009. Gas hydrate growth and dissociation in narrow pore networks: Capillary inhibition and hysteresis phenomena. In Long, D., et al. (eds.), *Sediment-Hosted Gas Hydrates: New Insights on Natural and Synthetic Systems*, Geol. Soc. Spec. Publ., 319, 145–159.

Berner, R.A., 1980. *Early diagenesis: A theoretical approach*. Princeton University Press, Princeton, N.J.

Bhatnagar, G., Chapman, W.G., Dickens, G.R., Dugan, B., Hirasaki, G.J., 2007. Generalization of gas hydrate distribution and saturation in marine sediments by scaling of thermodynamic and transport processes. *American Journal of Science*, 307(6), 861-900.

Bihani, A.D., 2016. *Pore size distribution and methane equilibrium conditions at Walker Ridge Block 313, northern Gulf of Mexico*. M.S. thesis, University of Texas at Austin, Austin, TX.

Bird, R.B., Stewart, W.E., Lightfoot, E.N. 2007. *Transport phenomena*, 2nd ed. John Wiley and Sons, New York, N.Y.

Boswell, R., Collett, T., Frye, M., McConnell, D., Shedd, W., Dufrene, R., Godfriaux, P., Mrozewski, S., Guerin, G., Cook, A., 2010. *Gulf of Mexico Gas Hydrate Joint Industry Project Leg II 2009 logging-while-drilling program: Technical summary*.

Boswell, R., Collett, T.S., Frye, M., Shedd, W., McConnell, D.R., Shelander, D., 2012. Subsurface gas hydrates in the northern Gulf of Mexico, *Marine and Petroleum Geology*, 34(1), 4-30.

Brooks, R.H., Corey, A.T., 1964. Hydraulic properties of porous media and their relation to drainage design. *Transactions of the ASAE*, 7(1), 26-28.

Carroll, J.J., Mather, A.E., 1997. A model for the solubility of light hydrocarbons in water and aqueous solutions of alkanolamines. *Chemical Engineering Science*, 52, 545-552.

Chaouachi, M., Falenty, A., Sell, K., Enzmann, F., Kersten, M., Haberthür, D., Kuhs, W.F., 2015. Microstructural evolution of gas hydrates in sedimentary matrices observed with synchrotron X-ray computed tomographic microscopy. *Geochemistry, Geophysics, Geosystems*, 16(6), 1711-1722.

Chapoy, A., Coquelet, C., Richon, D., 2004. Solubility and modeling of water in the gas phase of the methane/water binary system at temperatures from 283.08 to 318.12K and pressure up to 34.5 MPa. *Fluid Phase Equilibria*, 214(1), 101-117.

Civan, F., 2001. Scale effect on porosity and permeability: Kinetics, model, and correlation. *AIChE Journal*, 47(2), 271-287.

Claypool, G.E., Kaplan, I.R., 1974. The origin and distribution of methane in marine sediments. In Kaplan, I.R. (ed.), *Natural gases in marine sediments*, pp. 99–139, Plenum, New York, N.Y.

Clennell, M.B., Hovland, M., Booth, J. S., Henry, P., Winters, W.J., 1999. Formation of natural gas hydrates in marine sediments: 1. Conceptual model of gas hydrate growth conditioned by host sediment properties. *Journal of Geophysical Research: Solid Earth*, 104(B10), 22985-23003.

Collett, T.S., et al., 2008. *Results of the Indian National Gas Hydrate Program 01. Initial reports*. Directorate General of Hydrocarbons, Ministry of Petroleum and Natural Gas, New Delhi, India.

Cook, A.E., Malinverno, A., 2013. Short migration of methane into a gas hydrate-bearing sand layer at Walker Ridge, Gulf of Mexico. *Geochemistry, Geophysics, Geosystems*, 14(2), 283-291.

Cook, A.E., Anderson, B.I., Rasmus, J., Sun, K., Li, Q., Collett, T.S., Goldberg, D.S., 2012. Electrical anisotropy of gas hydrate bearing sand reservoirs in the Gulf of Mexico. *Marine and Petroleum Geology*, 34(1), 72-84.

Cook, A.E., Goldberg, D., Malinverno, A., 2014. Natural gas hydrates occupying fractures: A focus on non-vent sites on the Indian continental margin and the northern Gulf of Mexico. *Marine and Petroleum Geology*, 58, 278-291.

Dai, S., Seol, Y., 2014. Water permeability in hydrate-bearing sediments: A pore-scale study. *Geophysical Research Letters*, 41, 4176–4184.

Daigle, H., Dugan, B., 2010. Origin and evolution of fracture-hosted methane hydrate deposits. *Journal of Geophysical Research: Solid Earth*, 115(B11), B11103.

Daigle, H., Reece, J.S., 2015. Permeability of two-component granular materials. *Transport in Porous Media*, 106(3), 523-544.

Davie, M.K., Buffett, B.A., 2001. A numerical model for the formation of gas hydrate below the seafloor. *Journal of Geophysical Research: Solid Earth*, 106(B1), 497-514.

Flemings, P.B., Phillips, S.C, Collett, T., Cook, A., Boswell, R., and the UT-GOM2-1 Expedition Scientists, 2018. UT-GOM2-1 Hydrate Pressure Coring Expedition Summary. In Flemings, P.B., Phillips, S.C, Collett, T., Cook, A., Boswell, R., and the UT-GOM2-1 Expedition Scientists, UT-GOM2-1 Hydrate Pressure Coring Expedition Report: Austin, TX (University of Texas Institute for Geophysics, TX). https://ig.utexas.edu/energy/genesis-of-methane-hydrate-in-coarse-grained-systems/expedition-ut-gom2-1/reports/.

Frederick, J.M., Buffett, B.A., 2011. Topography- and fracture-driven fluid focusing in layered ocean sediments. *Geophysical Research Letters*, 38(8), L08614.

Frye, M., 2008. Preliminary evaluation of in-place gas hydrate resources: Gulf of Mexico Outer Continental Shelf. Minerals Management Service Report 2008-004. Available online at: http://www.boem.gov/uploadedFiles/BOEM/Oil_and_Gas_Energy_Program/Resource_Evaluation/Gas_Hydrates/MMS2008-004.pdf.

Frye, M., Shedd, W., Boswell, R., 2012. Gas hydrate resource potential in the Terrebonne Basin, Northern Gulf of Mexico. *Marine and Petroleum Geology*, 34(1), 150-168.

Fukusako, S., Yamada, M., 1993. Recent advances in research on water-freezing and ice-melting problems. *Experimental Thermal and Fluid Science*, 6(1), 90-105.

Handa, Y.P., 1986. Compositions, enthalpies of dissociation, and heat capacities in the range 85 to 270 K for clathrate hydrates of methane, ethane, and propane, and enthalpy of dissociation of isobutane hydrate, as determined by a heat-flow calorimeter. *The Journal of Chemical Thermodynamics*, 18(10), 915-921.

Hedges, J.I., Keil, R.G., 1995. Sedimentary organic matter preservation: an assessment and speculative synthesis. *Marine Chemistry*, 49(2-3), 81-115.

Henry, P., Thomas, M., Clennell, M.B., 1999. Formation of natural gas hydrates in marine sediments: 2. Thermodynamic calculations of stability conditions in porous sediments. *Journal of Geophysical Research: Solid Earth*, 104(B10), 23005-23022.

Hillman, J.I.T., Cook, A.E., Daigle, H., Nole, M., Malinverno, A., Meazell, K., Flemings, P.B., 2017. Gas hydrate reservoirs and gas migration mechanisms in the Terrebonne Basin, Gulf of Mexico. *Marine and Petroleum Geology*, 86, 1357-1373.

Hutchinson, D.R., et al., 2008. Site Selection for the DOE/JIP gas hydrate drilling in the northern Gulf of Mexico. 6th International Conference on Gas Hydrates, Vancouver, British Columbia, 6-10 July 2008.

Kang, N., Yoo, D., Yi, B., Park, S., 2016. Distribution and origin of seismic chimneys associated with gas hydrate using 2D multi-channel seismic reflection and well log data in the Ulleung Basin, East Sea. *Quaternary International*, 392, 99-111.

Kerkar, P.B., Horvat, K., Jones, K.W., Mahajan, D., 2014. Imaging methane hydrates growth dynamics in porous media using synchrotron X-ray computed microtomography. *Geochemistry, Geophysics, Geosystems*, 15(12), 4759-4768.

Kim, Y.S., Ryu, S.K., Yang, S.O., Lee, C.S., 2003. Liquid water-hydrate equilibrium measurements and unified predictions of hydrate-containing phase equilibria for methane, ethane, propane, and their mixtures. *Industrial & Engineering Chemistry Research*, 42(11), 2409-2414.

Kim, G.Y., Yi, B.Y., Yoo, D.G., Ryu, B.J., Riedel, M., 2011. Evidence of gas hydrate from downhole logging data in the Ulleung Basin, East Sea. *Marine and Petroleum Geology*, 28(10), 1979-1985.

Klauda, J.B., Sandler, S.I., 2001. Modeling gas hydrate phase equilibria in laboratory and natural porous media. *Industrial & Engineering Chemistry Research*, 40(20), 4197-4208.

Koh, C.A., Westacott, R.E., Zhang, W., Hirachand, K., Creek, J.L., Soper, A.K., 2002. Mechanisms of gas hydrate formation and inhibition. *Fluid Phase Equilibria*, 194-197, 143-151.

Kramer, K.V., Shedd, W.W., 2017. A 1.4-billion-pixel map of the Gulf of Mexico seafloor. *Eos*, 98,https://doi.org/10.1029/2017EO073557. Published on 24 May 2017.

Kumar, P., Collett, T.S., Vishwanath, K., Shukla, K.M., Nagalingam, J., Lall, M.V., Yamada, Y., Schultheiss, P., Holland, M., 2016. Gas hydrate-bearing sand reservoir systems in the offshore of India: Results of the India National Gas Hydrate Program Expedition 02. *Fire in the Ice*, 16(1), 1-8.

Lake, L.W., 1989. *Enhanced oil recovery*. Prentice-Hall, Upper Saddle River, N.J.

Lide, D.R., ed., 2004. *CRC handbook of chemistry and physics*, vol. 85. CRC Press, Boca Raton, FL.

Liu, X., Flemings, P.B., 2006. Passing gas through the hydrate stability zone at southern Hydrate Ridge, offshore Oregon. *Earth and Planetary Science Letters*, 241(1), 211-226.

Liu, X., Flemings, P.B., 2011. Capillary effects on hydrate stability in marine sediments. *Journal of Geophysical Research: Solid Earth*, 116(B7), B07102.

Malinverno, A., 2010. Marine gas hydrates in thin sand layers that soak up microbial methane. *Earth and Planetary Science Letters*, 292(3-4), 399-408.

Malinverno, A., Goldberg, D.S., 2015. Testing short-range migration of microbial methane as a hydrate formation mechanism: Results from Andaman Sea and Kumano Basin drill sites and global implications. *Earth and Planetary Science Letters*, 422, 105-114.

Malinverno, A., Cook, A.E., Daigle, H., Oryan, B., 2018. Glacial cycles influence marine methane hydrate formation. *Geophysical Research Letters*, 45(2), 724-732.

McConnell, D.R., Kendall, B.A., 2002. Images of the base of gas hydrate stability, Northwest Walker Ridge, Gulf of Mexico. Offshore Technology Conference, Houston, Texas, 6-9 May 2002, paper 14103.

McConnell, D.R., Boswell, R., Collett, T., Frye, M., Shedd, W., Guerin, G., Cook, A., Mrozewski, S., Dufrene, R., Godfriaux, P., 2010. Gulf of Mexico Gas Hydrate Joint Industy Project Leg II: Walker Ridge 313 Site Summary. Available online at: http://www.netl.doe.gov/technologies/oil-gas/futuresupply/methanehydrates/jiplegii-ir/

Miller, J.W., McGinley, J.J., Yaws, C.L., 1976a. Thermal-conductivities of liquids. *Chemical Engineering*, 83(23), 133-135.

Miller, J.W., Schorr, G.R., Yaws, C.L., 1976b. Heat-capacities of liquids. *Chemical Engineering*, 83(23), 129-131.

Moridis, G.J., Collett, T.S, Boswell, R., Kurihara, M., Reagan, M.T., Koh, C., Sloan, E.D., 2008. Toward production from gas hydrates: Current status, assessment of resources, and model-based evaluation of technology and potential. SPE Unconventional Resources Conference, Keystone, Colorado, 10-12 February 2008, paper SPE 114163.

Nole, M., Daigle, H., Cook, A.E., Malinverno, A., 2016. Short-range, overpressure-driven methane migration in coarse-grained gas hydrate reservoirs. *Geophysical Research Letters*, 43(18), 9500-9508.

Nole, M., Daigle, H., Cook, A.E., Hillman, J.I.T., Malinverno, A., 2017. Linking basin-scale and pore-scale gas hydrate distribution patterns in diffusion-dominated marine hydrate systems. *Geochemistry, Geophysics, Geosystems*, 18(2), 653-675.

Pohlman, J.W., Kaneko, M., Heuer, V.B., Coffin, R.B., Whiticar, M., 2009. Methane sources and production in the northern Cascadia margin gas hydrate system. *Earth and Planetary Science Letters*, 287(3-4), 504-512.

Pruess, K., Oldenburg, C.M., Moridis, G.J., 1999. *TOUGH2 user's guide version 2* (No. LBNL--43134). Ernest Orlando Lawrence Berkeley National Laboratory, Berkeley, CA.

Qin, F.G.F., Zhao, J.C., Russell, A.B., Chen, X.D., Chen, J.J., Robertson, L., 2003. Simulation and experiment of the unsteady heat transport in the onset time of nucleation and

crystallization of ice from the subcooled solution. *International Journal of Heat and Mass Transfer*, 46(17), 3221-3231.
Quintard, M., Whitaker, S., 1995. Local thermal equilibrium for transient heat conduction: theory and comparison with numerical experiments. *International Journal of Heat and Mass Transfer*, 38(15), 2779-2796.
Rempel, A.W., 2011. A model for the diffusive growth of hydrate saturation anomalies in layered sediments. *Journal of Geophysical Research: Solid Earth*, 116(B10), B10105.
Rempel, A.W., Buffett, B.A., 1997. Formation and accumulation of gas hydrate in porous media. *Journal of Geophysical Research: Solid Earth*, 102(B5), 10151-10164.
Rice, D.D., Claypool, G.E., 1981. Generation, accumulation, and resource potential of biogenic gas. *AAPG Bulletin*, 65(1), 5-25.
Rubey, W.W., Hubbert, M.K., 1959. Role of fluid pressure in mechanics of overthrust faulting: II. Overthrust belt in geosynclinal area of western Wyoming in light of fluid-pressure hypothesis. *Geological Society of America Bulletin*, 70(2), 167-206.
Selim, M.S., Sloan, E.D., 1989. Heat and mass transfer during the dissociation of hydrates in porous media. *AIChE Journal*, 35(6), 1049-1052.
Shedd, W., Boswell, R., Frye, M., Godfriaux, P., Kramer, K., 2012. Occurrence and nature of "bottom simulating reflectors" in the northern Gulf of Mexico. *Marine and Petroleum Geology*, 34(1), 31-40.
Sloan, E.D., Koh, C., 2007. *Clathrate hydrates of natural gases.* CRC Press, Boca Raton, FL.
Sun, R., Duan, Z., 2007. An accurate model to predict the thermodynamic stability of methane hydrate and methane solubility in marine environments. *Chemical Geology*, 244(1-2), 248-262.
Sun, X., 2005. *Modeling of hydrate formation and dissociation in porous media*. Ph.D. thesis, University of Houston, Houston, TX.
Sun, X., Mohanty, K.K., 2006. Kinetic simulation of methane hydrate formation and dissociation in porous media. *Chemical Engineering Science*, 61(11), 3476-3495.
Tamaki, M., Fujii, T., Suzuki, K., 2017. Characterization and prediction of the gas hydrate reservoir at the second offshore gas production test site in the eastern Nankai Trough, Japan. *Energies*, 10(10), 1678.
Tester, J.W., Modell, M., 1997. *Thermodynamics and its applications*, 3rd ed. Prentice Hall, Upper Saddle River, N.J.
Tsuji, Y., Ishida, H., Nakamizu, M., Matsumoto, R., Shimizu, S., 2008. Overview of the MITI Nankai Trough wells: A milestone in the evaluation of methane hydrate resources. *Resource Geology*, 54(1), 3-10.
Waseda, A., 1998. Organic carbon content, bacterial methanogenesis, and accumulation processes of gas hydrates in marine sediments. *Geochemical Journal*, 32(3), 143-157.
Webb, S.W., 1998. Gas-Phase Diffusion in porous media-evaluation of an advective-dispersive formulation and the dusty-gas model for binary mixtures. *Journal of Porous Media*, 1(2), 187-199.
Yaws, C.L., 1995. *Handbook of transport property data: Viscosity, thermal conductivity, and diffusion coefficients of liquids and gases*. Gulf Publishing Company, Houston, TX.
You, K., Flemings, P.B., 2018. Methane hydrate formation in thick sand reservoirs: 1. Short-range methane diffusion. *Marine and Petroleum Geology*, 89, 428-442.

List of acronyms and abbreviations

API: American Petroleum Institute gamma ray units
BHSZ: Base of the methane hydrate stability zone
BSR: Bottom-simulating reflection
GC955: Green Canyon Block 955
GOM: Gulf of Mexico
GOM2: Genesis of Methane Hydrate in Coarse-Grained Systems: Northern Gulf of Mexico Slope
GR: Gamma ray
HFZ: Hydrate-free zone
IODP: Integrated Ocean Drilling Program
JIP: Chevron-led Gulf of Mexico Gas Hydrate Joint Industry Project
K-G: Krishna-Godavari
LWD: Logging-while-drilling
MHSZ: Methane hydrate stability zone
NGHP: India National Gas Hydrate Program
NMR: Nuclear magnetic resonance
RES: Resistivity
WR313: Walker Ridge Block 313